Available online at www.sciencedirect.com
ScienceDirect
Journal of Sound and Vibration 320 (2009) 1100–1130
JOURNAL OF SOUND AND VIBRATION
www.elsevier.com/locate/jsvi

An edge-based smoothed finite element method (ES-FEM) for static, free and forced vibration analyses of solids

G.R. Liu[a,b], T. Nguyen-Thoi[a,*], K.Y. Lam[c]

[a]*Center for Advanced Computations in Engineering Science (ACES), Department of Mechanical Engineering, National University of Singapore, 9 Engineering Drive 1, Singapore 117576, Singapore*
[b]*Singapore-MIT Alliance (SMA), E4-04-10, 4 Engineering Drive 3, Singapore 117576, Singapore*
[c]*School of Mechanical and Aerospace Engineering, Nanyang Technological University, 50 Nanyang Avenue, Singapore 639798, Singapore*

Received 26 January 2008; received in revised form 26 August 2008; accepted 26 August 2008
Handling Editor: L.G. Tham
Available online 10 October 2008

Abstract

This paper presents an edge-based smoothed finite element method (ES-FEM) to significantly improve the accuracy of the finite element method (FEM) without much changing to the standard FEM settings. The ES-FEM can use different shape of elements but prefers triangular elements that can be much easily generated automatically for complicated domains. In the ES-FEM, the system stiffness matrix is computed using strains smoothed over the smoothing domains associated with the edges of the triangles. Intensive numerical results demonstrated that the ES-FEM possesses the following excellent properties: (1) the ES-FEM model possesses a close-to-exact stiffness: it is much softer than the "overly-stiff" FEM and much stiffer than the "overly-soft" NS-FEM model; (2) the results are often found superconvergence and ultra-accurate: much more accurate than the linear triangular elements of FEM and even more accurate than those of the FEM using quadrilateral elements with the same sets of nodes; (3) there are no spurious non-zeros energy modes found and hence the method is also temporally stable and works well for vibration analysis and (4) the implementation of the method is straightforward and no penalty parameter is used, and the computational efficiency is better than the FEM using the same sets of nodes. In addition, a novel domain-based selective scheme is proposed leading to a combined ES/NS-FEM model that is immune from volumetric locking and hence works very well for nearly incompressible materials. These properties of the ES-FEM are confirmed using examples of static, free and forced vibration analyses of solids.

1. Introduction

The strain smoothing technique has been proposed by Chen et al. [1] to stabilize the solutions in the nodal integrated meshfree methods and then applied to the natural element method [2]. Liu et al. have applied this technique and extended it to a generalized smoothing technique allowing discontinuous displacement functions [22]. The generalized smoothing technique forms the theoretical foundation for the linear conforming point interpolation method (LC-PIM) using incompatible PIM shape functions created by simple

*Corresponding author. Tel.: +65 9860 4962.
E-mail address: g0500347@nus.edu.sg (T. Nguyen-Thoi).

0022-460X/$ - see front matter © 2008 Elsevier Ltd. All rights reserved.
doi:10.1016/j.jsv.2008.08.027

point interpolations based on a set of local nodes that can overlap [3]. Since the smoothed operation in the LC-PIM is node-based, it is also called node-based smoothed PIM (or NS-PIM). The linearly conforming radial point interpolation method (LC-RPIM or NS-RPIM) using RPIM shape functions has also been formulated that works for extremely irregularly distributed nodes [4]. Applying the strain smoothing technique to the finite elements leads to the element-based smoothed finite element method (SFEM) [5–7] and the node-based smoothed finite element method (NS-FEM) [8]. The SFEM uses cell-based smoothing domains created by further dividing the elements (quadrilateral or n-sided polygonal) into one or more smoothing cells (SC), as shown in Fig. 1. For the quadrilateral elements, when the number of SC of the elements equals 1, the SFEM solution is proven *variationally consistent* and has the same properties with those of FEM using reduced integration; when SC approaches infinity, the SFEM solution will approach the solution of the standard displacement compatible FEM model. It is suggested that there exists an optimal number of SC such that the SFEM solution is closest to the exact solution. In the contrast, in the NS-FEM, the strain smoothing domains and the integration of the weak form are performed over the domains associated with nodes, and methods can be applied easily to triangular, 4-node quadrilateral and even n-sided polygonal elements. For n-sided polygonal elements, the domain $\Omega^{(k)}$ associated with the node k is created by connecting sequentially the mid-edge-point to the central points of the surrounding n-sided polygonal elements of the node k as shown in Fig. 2. When only linear triangular elements are used, the NS-FEM produces the same results as the method proposed by Dohrmann [9] or to the NS-PIM [3] using linear shape functions. Liu et al. [10,11] have provided an intuitive explanation and showed numerically that the NS-PIM can produce an upper bound to the exact solution in the strain energy, when a reasonably fine mesh is used. The upper bound property was also found in the NS-FEM [8]. Both upper and lower bounds in the strain energy for elastic solid mechanics problems can now be obtained by combining the NS-FEM with the SFEM (for n-sided polygonal elements) or with the FEM (for triangular or 4-node quadrilateral elements). In addition, a nearly exact solution in strain energy using triangular and tetrahedral elements is also proposed by Liu et al. [24] by combining a scale factor $\alpha \in [0, 1]$ with the NS-FEM and the FEM to give a so-called the alpha Finite Element Method (αFEM). However, it is also found that the NS-FEM behaves "overly-soft" in contrary to the compatible FEM mode that is known "overly-stiff". The overly-soft behavior leads to instability similar to those found in the nodal integration methods [12–14]. The instability can be clearly shown as spurious non-zero energy modes in free vibration analyses, and as numerically unstable solution in forced vibration analyses.

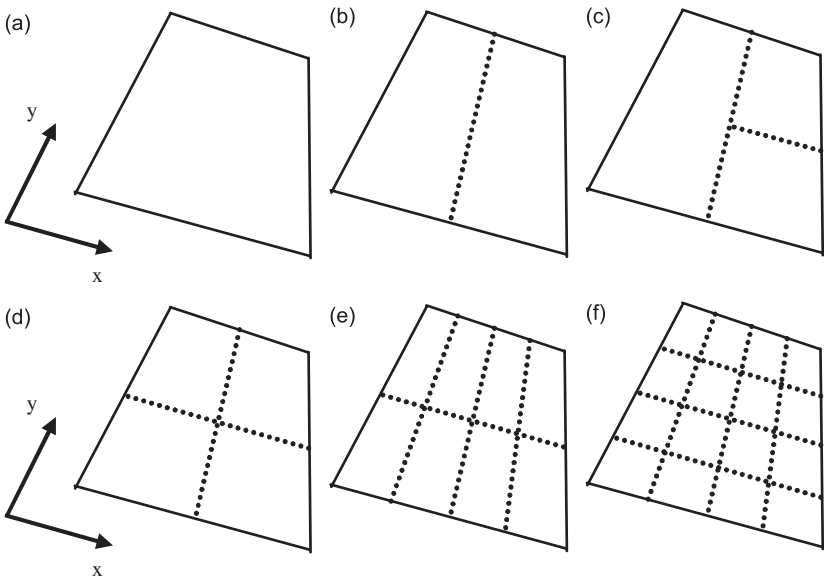

Fig. 1. Division of element into the smoothing cells (SC) in the SFEM. (a) SC = 1, (b) SC = 2, (c) SC = 3, (d) SC = 4, (e) SC = 8 and (f) SC = 16.

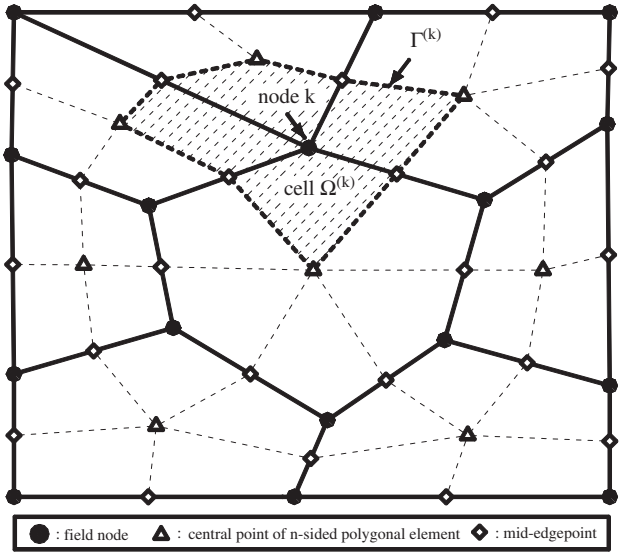

Fig. 2. *n*-Sided polygonal elements and the smoothing domains associated with nodes in the NS-FEM.

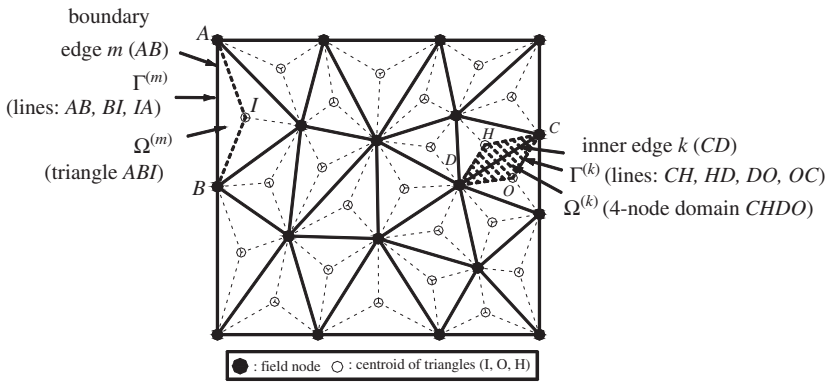

Fig. 3. Triangular elements and the smoothing domains associated with edges in the ES-FEM.

In this paper, we proposed a novel edge-based smoothed finite element method (ES-FEM) that is stable (no spurious non-zero energy modes) and more accurate compared to above mentioned methods including the FEM. In the ES-FEM, strain smoothing domains and the integration of the weak form are based on domains associated with edges of the elements. The smoothing domain of an edge is created by connecting two endpoints of the edge to two centroids of two adjacent elements that can be triangular, quadrilateral, or generally polygonal elements as shown in Figs. 3 and 4. The numerical results using triangular elements demonstrated that the ES-FEM gives very accurate solution and is even more accurate than the standard FEM using quadrilateral elements for both 2D static, free and forced vibration analyses of solid mechanics problems.

A novel domain-based selective scheme is also proposed in this paper leading to a combined ES/NS-FEM model that is immune from the volumetric locking, and works very well for solids of nearly incompressible materials. Most importantly, the present ES-FEM method eliminates spurious non-zero energy modes and hence is well suited for dynamics problems. The method does not use any penalty parameters and can be easily developed for 3D problems using tetrahedral elements. In addition, a mesh of mixed general *n*-sided polygonal elements (including triangular elements) can be used in an ES-FEM model, and hence relieve the burden on the generation of high quality meshes required in FEM.

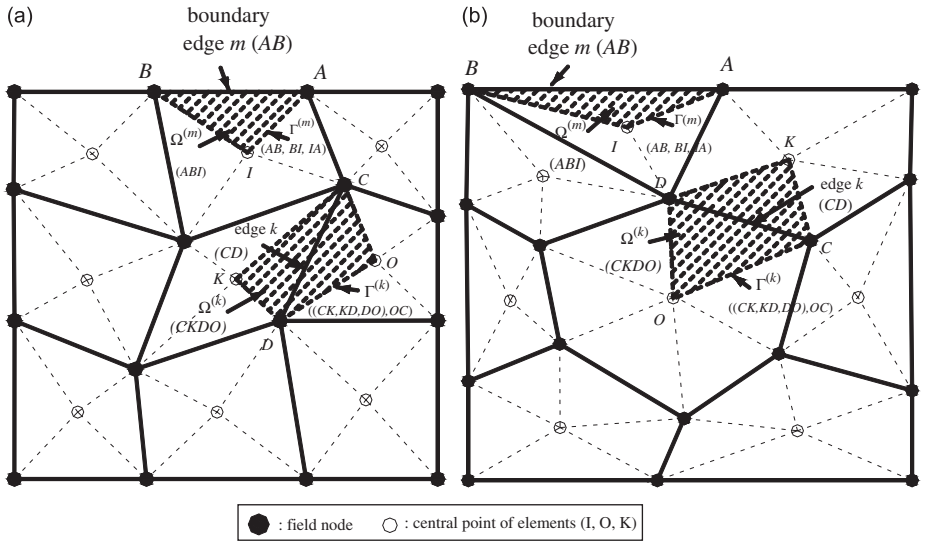

Fig. 4. Domain discretization and the smoothing domains associated with edges in the ES-FEM. (a) Quadrilateral elements and (b) n-sided polygonal elements.

2. The idea and formulation of the ES-FEM

This section formulates the ES-FEM for 2D problems using triangular elements. The formulation is largely the same as that in the FEM, except the integration procedure of calculating the stiffness matrix.

Consider a deformable body occupying domain Ω in motion, subjected to body forces $\mathbf{b}$, external applied tractions $\mathbf{t}$ on boundary Γ_t and displacement boundary conditions $\mathbf{u} = \bar{\mathbf{u}}$ on Γ_u. It undergoes arbitrary virtual displacements $\delta\mathbf{d}$ which accordingly give rise to compatible virtual strains $\delta\boldsymbol{\varepsilon}$ and internal displacements $\delta\mathbf{u}$. If the inertial and damping forces are also considered in the dynamic equilibrium equations, the principle of virtual work requires that

$$\int_{\Omega} \delta\boldsymbol{\varepsilon}^{\mathrm{T}} \mathbf{D}\boldsymbol{\varepsilon}\, \mathrm{d}\Omega - \int_{\Omega} \delta\mathbf{u}^{\mathrm{T}}[\mathbf{b} - \rho\ddot{\mathbf{u}} - c\dot{\mathbf{u}}]\, \mathrm{d}\Omega - \int_{\Gamma_t} \delta\mathbf{u}^{\mathrm{T}}\mathbf{t}\, \mathrm{d}\Gamma = 0 \tag{1}$$

where $\mathbf{D}$ is a matrix of material constants that is symmetric positive definite (SPD).

By means of the spatial discretization procedure in the FEM [15–17], the problem domain is divided into N_e elements. The virtual displacements and the compatible strains $\boldsymbol{\varepsilon} = \nabla_s \mathbf{u}$ within any element can be written as

$$\delta\mathbf{u}^h = \sum_{I=1}^{\mathrm{NP}} \mathbf{N}_I \delta\mathbf{d}_I, \quad \mathbf{u}^h = \sum_{I=1}^{\mathrm{NP}} \mathbf{N}_I \mathbf{d}_I \tag{2}$$

$$\delta\boldsymbol{\varepsilon}^h = \sum_{I} \mathbf{B}_I \delta\mathbf{d}_I, \quad \boldsymbol{\varepsilon}^h = \sum_{I} \mathbf{B}_I \mathbf{d}_I \tag{3}$$

where NP is the number of the nodal variables of the element, $\mathbf{d}_I = [u_I\ v_I]^{\mathrm{T}}$ is the nodal displacement vector, $\mathbf{N}_I = \begin{bmatrix} N_I & 0 \\ 0 & N_I \end{bmatrix}$ is the shape function matrix and $\mathbf{B}$ is the standard (compatible) displacement gradient matrix. In 2D linear elastic problems it is given as

$$\mathbf{B}_I = \begin{bmatrix} N_{I'x} & 0 \\ 0 & N_{I'y} \\ N_{I'y} & N_{I'x} \end{bmatrix} \tag{4}$$

The energy assembly process gives

$$\int_{\Omega} \delta \mathbf{d}^{\mathrm{T}} \mathbf{B}^{\mathrm{T}} \mathbf{D} \boldsymbol{\varepsilon} \, \mathrm{d}\Omega - \int_{\Omega} \delta \mathbf{d}^{\mathrm{T}} \mathbf{N}^{\mathrm{T}} [\mathbf{b} - \rho \ddot{\mathbf{u}} - c\dot{\mathbf{u}}] \, \mathrm{d}\Omega - \int_{\Gamma_t} \delta \mathbf{d}^{\mathrm{T}} \mathbf{N}^{\mathrm{T}} \mathbf{t} \, \mathrm{d}\Gamma = 0 \tag{5}$$

Since the expressions hold for any arbitrary virtual displacements $\delta \mathbf{d}$, we obtain

$$\int_{\Omega} \mathbf{B}^{\mathrm{T}} \mathbf{D} \boldsymbol{\varepsilon} \, \mathrm{d}\Omega - \int_{\Omega} \mathbf{N}^{\mathrm{T}} [\mathbf{b} - \rho \ddot{\mathbf{u}} - c\dot{\mathbf{u}}] \, \mathrm{d}\Omega - \int_{\Gamma_t} \mathbf{N}^{\mathrm{T}} \mathbf{t} \, \mathrm{d}\Gamma = 0 \tag{6}$$

The resultant discrete governing equation can be written as

$$\mathbf{M}\ddot{\mathbf{d}} + \mathbf{C}\dot{\mathbf{d}} + \mathbf{K}\mathbf{d} = \mathbf{f} \tag{7}$$

where $\mathbf{d}$ is the vector of general nodal displacements and

$$\mathbf{K} = \int_{\Omega} \mathbf{B}^{\mathrm{T}} \mathbf{D} \mathbf{B} \, \mathrm{d}\Omega \tag{8}$$

$$\mathbf{f} = \int_{\Omega} \mathbf{N}^{\mathrm{T}} \mathbf{b} \, \mathrm{d}\Omega + \int_{\Gamma_t} \mathbf{N}^{\mathrm{T}} \mathbf{t} \, \mathrm{d}\Gamma \tag{9}$$

$$\mathbf{M} = \int_{\Omega} \mathbf{N}^{\mathrm{T}} \boldsymbol{\rho} \mathbf{N} \, \mathrm{d}\Omega \tag{10}$$

$$\mathbf{C} = \int_{\Omega} \mathbf{N}^{\mathrm{T}} \mathbf{c} \mathbf{N} \, \mathrm{d}\Omega \tag{11}$$

It is clear that the formulation given above is the same as that of standard FEM. Similar to the standard FEM, the ES-FEM uses a mesh of elements. When triangular elements are used, the shape functions used in the ES-FEM is also the same as that in FEM.

In the ES-FEM, however, we do not use the compatible strains (3) but strains "smoothed" over local smoothing domains, and naturally the integration related to the stiffness matrix $\mathbf{K}$ is no longer based on elements, but these smoothing domains. These local smoothing domains are constructed based on edges of the elements such that $\Omega = \Omega^{(1)} \cup \Omega^{(2)} \cup \cdots \cup \Omega^{(N_s)}$ and $\Omega^{(i)} \cup \Omega^{(j)} \neq \emptyset$, $i \neq j$, in which N_s is the total number of edges (sides) located in the entire problem domain. For triangular elements, the smoothing domain $\Omega^{(k)}$ associated with the edge k is created by connecting two endpoints of the edge to two centroids of two adjacent elements as shown in Fig. 3. Extending the smoothing domain $\Omega^{(k)}$ associated with the edge k to quadrilateral or n-sided polygonal elements is straightforward as shown in Fig. 4.

Using the edge-based smoothing domains, *smoothed* strains can now be obtained using the *compatible* strains $\boldsymbol{\varepsilon} = \nabla_s \mathbf{u}$ through the following smoothing operation over domain $\Omega^{(k)}$ associated with edge k:

$$\tilde{\boldsymbol{\varepsilon}}_k = \int_{\Omega^{(k)}} \boldsymbol{\varepsilon}(\mathbf{x}) \Phi_k(\mathbf{x}) \, \mathrm{d}\Omega = \int_{\Omega^{(k)}} \nabla_s \mathbf{u}(\mathbf{x}) \Phi_k(\mathbf{x}) \, \mathrm{d}\Omega \tag{12}$$

where $\Phi_k(\mathbf{x})$ is a given smoothing function that satisfies at least unity property:

$$\int_{\Omega^{(k)}} \Phi_k(\mathbf{x}) \, \mathrm{d}\Omega = 1 \tag{13}$$

In this work, we use the simplest local constant smoothing function

$$\Phi_k(\mathbf{x}) = \begin{cases} 1/A^{(k)}, & \mathbf{x} \in \Omega^{(k)} \\ 0, & \mathbf{x} \notin \Omega^{(k)} \end{cases} \tag{14}$$

where $A^{(k)}$ is the area of the smoothing domain $\Omega^{(k)}$ and is calculated by

$$A^{(k)} = \int_{\Omega^{(k)}} \mathrm{d}\Omega = \frac{1}{3} \sum_{j=1}^{N_e^{(k)}} A_e^{(j)} \tag{15}$$

where $N_e^{(k)}$ is the number of elements around the edge k ($N_e^{(k)}=1$ for the boundary edges and $N_e^{(k)}=2$ for inner edges as shown in Fig. 3) and $A_e^{(j)}$ is the area of the jth element around the edge k.

Using the constant smoothing function (14), the smoothed strains obtained using Eq. (12) are constant in the smoothing domain. Therefore, the stiffness matrix $\mathbf{K}$ in Eq. (8) becomes the *smoothed* stiffness matrix $\tilde{\mathbf{K}}$ in the ES-FEM, and is assembled by a similar process as in the FEM:

$$\tilde{\mathbf{K}}=\sum_{k=1}^{N_s}\tilde{\mathbf{K}}_{(k)} \tag{16}$$

where $\tilde{\mathbf{K}}_{(k)}$ is the smoothed stiffness matrix calculated on the smoothing domains $\Omega^{(k)}$ associated with the edge k. The details of calculating $\tilde{\mathbf{K}}_{(k)}$ are given below.

Substituting Eq. (2) into Eq. (12), the smoothed strain on the domain $\Omega^{(k)}$ associated with edge k can be written in the following matrix form of nodal displacements:

$$\tilde{\boldsymbol{\varepsilon}}_k=\sum_{I\in N_n^{(k)}}\tilde{\mathbf{B}}_I(\mathbf{x}_k)\mathbf{d}_I \tag{17}$$

where $N_n^{(k)}$ is the total number of nodes of elements containing the common edge i ($N_n^{(k)}=3$ for boundary edges and $N_n^{(k)}=4$ for inner edges as shown in Fig. 3) and $\tilde{\mathbf{B}}_I(\mathbf{x}_k)$, that is termed as the *smoothed strain matrix* on the domain $\Omega^{(k)}$, is calculated numerically by an assembly process similarly as in the FEM

$$\tilde{\mathbf{B}}_I(\mathbf{x}_k)=\frac{1}{A^{(k)}}\sum_{j=1}^{N_e^{(k)}}\frac{1}{3}A_e^{(j)}\mathbf{B}_j \tag{18}$$

where $\mathbf{B}_j$ is the strain gradient matrix of the jth element around the edge k.

Due to the use of the triangular elements with the linear shape functions, the entries of matrix $\mathbf{B}_j$ are constants, and so are the entries of matrix $\tilde{\mathbf{B}}_I(\mathbf{x}_k)$. Now, the smoothing stiffness matrix $\tilde{\mathbf{K}}_{(k)}$ in Eq. (16) is calculated by

$$\tilde{\mathbf{K}}_{(k)}=\int_{\Omega^{(k)}}\tilde{\mathbf{B}}_I^{\mathrm{T}}\mathbf{D}\tilde{\mathbf{B}}_J\,\mathrm{d}\Omega=\tilde{\mathbf{B}}_I^{\mathrm{T}}\mathbf{D}\tilde{\mathbf{B}}_J A^{(k)} \tag{19}$$

Note that with this formulation, only the area and the usual "compatible" strain matrices $\mathbf{B}_j$ of triangular elements are needed to calculate the system stiffness matrix for the ES-FEM. This formulation is quite straightforward to extend for the 3D problems using tetrahedral elements.

Applying the divergence theorem, the smoothed strain matrix $\tilde{\mathbf{B}}_I(\mathbf{x}_k)$ on the domain $\Omega^{(k)}$ can be calculated in another way by

$$\tilde{\mathbf{B}}_I(\mathbf{x}_k)=\begin{bmatrix}\tilde{b}_{Ix}(\mathbf{x}_k) & 0\\ 0 & \tilde{b}_{Iy}(\mathbf{x}_k)\\ \tilde{b}_{Iy}(\mathbf{x}_k) & \tilde{b}_{Ix}(\mathbf{x}_k)\end{bmatrix} \tag{20}$$

with

$$\tilde{b}_{Ih}(\mathbf{x}_k)=\frac{1}{A^{(k)}}\int_{\Gamma^{(k)}}N_I(\mathbf{x})n_h^{(k)}(\mathbf{x})\,\mathrm{d}\Gamma\quad(h=x,y) \tag{21}$$

where $\Gamma^{(k)}$ is the boundary of the smoothing domain $\Omega^{(k)}$ as shown in Fig. 3 and $\mathbf{n}^{(k)}(\mathbf{x})$ is the outward normal vector matrix on the boundary $\Gamma^{(k)}$ and has the form

$$\mathbf{n}^{(k)}(\mathbf{x})=\begin{bmatrix}n_x^{(k)} & 0\\ 0 & n_y^{(k)}\\ n_y^{(k)} & n_x^{(k)}\end{bmatrix} \tag{22}$$

When a linear compatible displacement field along the boundary $\Gamma^{(k)}$ is used, one Gaussian point is sufficient for line integration along each segment of boundary $\Gamma_i^{(k)}$ of $\Omega^{(k)}$, the above equation can be further

simplified to its algebraic form

$$\tilde{b}_{Ih}(\mathbf{x}_k) = \frac{1}{A^{(k)}} \sum_{i=1}^{M} N_I(\mathbf{x}_i^{\mathrm{GP}}) n_{ih}^{(k)} l_i^{(k)} \quad (h = x, y) \tag{23}$$

where M is the total number of the boundary segments of $\Gamma_i^{(k)}$, $\mathbf{x}^{\mathrm{GP}}{}_i$ is the midpoint (Gaussian point) of the boundary segment of $\Gamma_i^{(k)}$, whose length and outward unit normal are denoted as $l_i^{(k)}$ and $n_{ih}^{(k)}$, respectively.

Eq. (23) implies that only shape function values at some particular points along segments of boundary $\Gamma_i^{(k)}$ are needed and no explicit analytical form is required. This gives tremendous freedom in shape function construction, and the shape functions do not need to form explicitly and their values at interest points can be obtained by simple interpolation [7].

Note that using Eq. (20) to calculate $\tilde{\mathbf{B}}_I(\mathbf{x}_k)$, it is straightforward to extend the ES-FEM for the domain discretized by quadrilateral or n-sided polygonal elements, and all one needs to do is to create edge-based smoothing domains as shown in Fig. 4.

Finally, we note that the trial function $\mathbf{u}^h(\mathbf{x})$ is the same as that given in Eq. (2) and therefore the force vector $\mathbf{f}$, mass matrix $\mathbf{M}$ and damping matrix $\mathbf{C}$ in the ES-FEM are calculated in the same way as in the FEM. In other words, the ES-FEM changes only the stiffness matrix. The spatial stability and convergence can be proven in the same manner presented in [10] using the argument of orthogonal conditions within the frame work of weak formulation. An alternative proof based on so-called weakened weak formulation using $\mathbf{G}$ space theory is presented in [23], which is more general and applicable for models using incompatible shape functions.

3. Forced and free vibration analyses

Using Eqs. (16) and (19), the discretized equation system in the ES-FEM can be expressed as

$$\mathbf{M}\ddot{\mathbf{d}} + \mathbf{C}\dot{\mathbf{d}} + \tilde{\mathbf{K}}\mathbf{d} = \mathbf{f} \tag{24}$$

For simplicity, the Rayleigh damping is used, and the damping matrix $\mathbf{C}$ is assumed to be a linear combination of $\mathbf{M}$ and $\tilde{\mathbf{K}}$,

$$\mathbf{C} = \alpha\mathbf{M} + \beta\tilde{\mathbf{K}} \tag{25}$$

where α and β are the Rayleigh damping coefficients.

Many schemes can be used to solve the second-order time dependent problems, such as the Newmark method, Crank–Nicholson method, etc. [19]. In this work, the Newmark method is used. When the state at $t = t_0$ $(\mathbf{d}_0, \dot{\mathbf{d}}_0, \ddot{\mathbf{d}}_0)$ is known, we aim to find the new state at $t_1 = t_0 + \theta\,\Delta t$ $(\mathbf{d}_1, \dot{\mathbf{d}}_1, \ddot{\mathbf{d}}_1)$ where $0.5 \leqslant \theta \leqslant 1$, using the following formulations:

$$\begin{aligned}\left[\left(\alpha + \frac{1}{\theta\,\Delta t}\right)\mathbf{M} + (\beta + \theta\,\Delta t)\mathbf{K}\right]\mathbf{d}_1 &= \theta\,\Delta t\,\mathbf{f}_1 + (1-\theta)\Delta t\,\mathbf{f}_0 \\ &+ \left(\alpha + \frac{1}{\theta\,\Delta t}\right)\mathbf{M}\mathbf{d}_0 + \frac{1}{\theta}\mathbf{M}\dot{\mathbf{d}}_0 + [\beta - (1-\theta)\Delta t]\mathbf{K}\mathbf{d}_0\end{aligned} \tag{26}$$

$$\dot{\mathbf{d}}_1 = \frac{1}{\theta\,\Delta t}(\mathbf{d}_1 - \mathbf{d}_0) - \frac{1-\theta}{\theta}\dot{\mathbf{d}}_0 \tag{27}$$

$$\ddot{\mathbf{d}}_1 = \frac{1}{\theta\,\Delta t}(\dot{\mathbf{d}}_1 - \dot{\mathbf{d}}_0) - \frac{1-\theta}{\theta}\ddot{\mathbf{d}}_0 \tag{28}$$

Without damping and forcing terms, Eq. (24) now reduces to a homogenous equation:

$$\mathbf{M}\ddot{\mathbf{d}} + \tilde{\mathbf{K}}\mathbf{d} = \mathbf{0} \tag{29}$$

A general solution of such a homogenous equation can be written as

$$\mathbf{d} = \bar{\mathbf{d}}\,\exp(\mathrm{i}\omega t) \tag{30}$$

where t indicates time, $\bar{\mathbf{d}}$ is the eigenvector and ω is natural frequency. On its substitution into Eq. (29), the natural frequency ω can be found by solving the following eigenvalue equation:

$$(-\omega^2\mathbf{M}+\tilde{\mathbf{K}})\bar{\mathbf{d}}=\mathbf{0} \tag{31}$$

4. A domain-based selective scheme: a combined ES/NS-FEM model

Volumetric locking appears when the Poisson's ratio approaches to 0.5. The application of selective formulations in the conventional FEM [20] has been found effectively to overcome such a locking and hence the similar idea is employed in this paper. However, different from the FEM using selective integration [20], our selective scheme will use two different types of smoothing domains selectively for two different material "parts" (μ-part and λ-part). Since the node-based smoothing domains used in NS-FEM were found effective in overcoming volumetric locking [8], and the λ-part is known as the culprit of the volume locking, we use node-based domains for the λ-part and edge-based domains for the μ-part. The details are given below.

The material property matrix $\mathbf{D}$ for isotropic materials is first decomposed into

$$\mathbf{D}=\mathbf{D}_1+\mathbf{D}_2 \tag{32}$$

where $\mathbf{D}_1$ relates to the shearing modulus $\mu=E/[2(1+v)]$ and hence is termed as μ-part of $\mathbf{D}$, and $\mathbf{D}_2$ relates to the Lame's parameter $\lambda=2v\mu/(1-2v)$ and hence is termed as λ-part of $\mathbf{D}$. For plane strain cases, we have

$$\mathbf{D}=\begin{bmatrix}\lambda+2\mu & \lambda & 0\\ \lambda & \lambda+2\mu & 0\\ 0 & 0 & \mu\end{bmatrix}=\mu\begin{bmatrix}2 & 0 & 0\\ 0 & 2 & 0\\ 0 & 0 & 1\end{bmatrix}+\lambda\begin{bmatrix}1 & 1 & 0\\ 1 & 1 & 0\\ 0 & 0 & 0\end{bmatrix}=\mathbf{D}_1+\mathbf{D}_2 \tag{33}$$

and for axis-symmetric problems:

$$\mathbf{D}=\mu\begin{bmatrix}2 & 0 & 0 & 0\\ 0 & 2 & 0 & 0\\ 0 & 0 & 1 & 0\\ 0 & 0 & 0 & 2\end{bmatrix}+\lambda\begin{bmatrix}1 & 1 & 0 & 1\\ 1 & 1 & 0 & 1\\ 0 & 0 & 0 & 0\\ 1 & 1 & 0 & 1\end{bmatrix}=\mathbf{D}_1+\mathbf{D}_2 \tag{34}$$

In our domain-based selective scheme proposed, we use the NS-FEM to calculate the stiffness matrix related to λ-part and the ES-FEM to calculate the one related to the μ-part. The stiffness matrix of the combined ES/NS-FEM model becomes

$$\tilde{\mathbf{K}}=\underbrace{\sum_{i=1}^{N_s}(\tilde{\mathbf{B}}_1^i)^{\mathrm{T}}\mathbf{D}_1\tilde{\mathbf{B}}_1^iA_1^i}_{\tilde{\mathbf{K}}_1^{\text{ES-FEM}}}+\underbrace{\sum_{j=1}^{N_n}(\tilde{\mathbf{B}}_2^j)^{\mathrm{T}}\mathbf{D}_2\tilde{\mathbf{B}}_2^jA_2^j}_{\tilde{\mathbf{K}}_2^{\text{NS-FEM}}} \tag{35}$$

where $\tilde{\mathbf{B}}_1^i$ and A_1^i are the smoothed strain matrix and area of the smoothing domain $\Omega_s^{(i)}$ associated with edge i, correspondingly, $\tilde{\mathbf{B}}_2^j$ and A_2^j are the smoothed strain matrix and area of the smoothing domain $\Omega_n^{(j)}$ associated with node j, correspondingly, and N_n is the total number of nodes located in the entire problem domain.

5. Numerical implementation

5.1. Stability of the ES-FEM

In the NS-FEM [8] (or LC-PIM [3]), smoothing domains associated with the node is employed to calculate the stiffness matrix. This works well for static problems. However, for vibration analysis, the

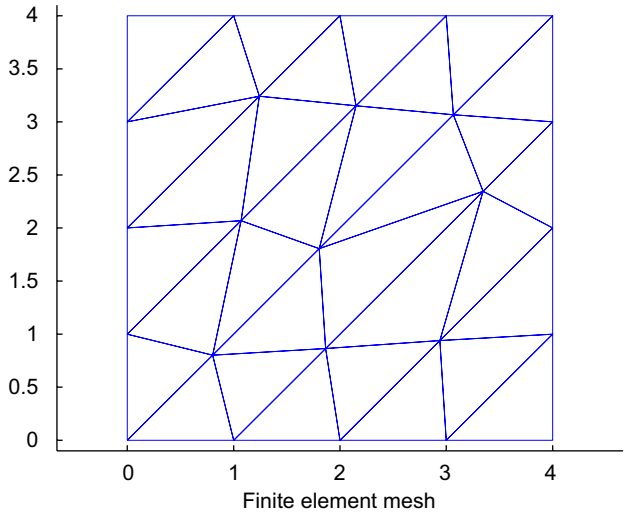

Fig. 5. The mesh discretization for standard patch test.

NS-FEM (or LC-PIM) is unstable because of the presence of spurious non-zero energy modes. This is due to the under-integration of the weak form inherent in the nodal integration approaches [12–14].

In the standard FEM using triangular meshes and linear shape functions, the integration on the weak form is based on elements. For each element, only one Gauss point is needed to calculate. This implies that the number of Gauss points to calculate equals to the number of elements of the problem. Such an FEM model is known stable in dynamic analysis and has no spurious non-zero energy modes.

In the ES-FEM using triangular meshes, the smoothing domains used are associated with edges and the strain (or stress) on each domain is constant. Therefore, each domain is considered equivalent to using one Gauss point to calculate the weak form. Because the number of edges is always larger than the number of elements in any meshes, or in other words, the number of Gauss points to calculate the weak form in the ES-FEM is larger than that in the FEM, the ES-FEM is also very stable and has no spurious non-zero energy modes. Therefore, the ES-FEM is well suited for the dynamic analysis.

5.2. Standard patch test

Satisfaction of the standard patch test requires that the displacements of all the interior nodes of the patch follow "exactly" (to machine precision) the same linear function of the imposed displacement on the boundary of the patch. A domain discretization of a square patch using 32 irregular triangular elements is shown in Fig. 5. The following error norm in displacements is used to examine the computed results:

$$e_d = \frac{\sum_{i=1}^{\text{ndof}} |u_i - u_i^h|}{\sum_{i=1}^{\text{ndof}} |u_i|} \times 100\% \tag{36}$$

where u_i is the exact solution, u_i^h is the numerical solution and ndof is the number of degrees of freedom (dofs) of the system.

The parameters are taken as $E = 100$, $v = 0.3$ and linear displacement field is given by

$$\begin{aligned} u &= x \\ v &= y \end{aligned} \tag{37}$$

It is found that the ES-FEM can pass the standard patch test within machine precision with the error norm in displacements: $e_d = 1.28\text{e}{-11}$ (%).

5.3. Mass matrix

In dynamic analysis, the lumped mass matrix for the linear triangular element is

$$[\mathbf{M}]^e = \frac{\rho t A}{3}[\mathbf{I}] \tag{38}$$

where [**I**] is the identity matrix of size 6, A is the area of the element, ρ and t are the mass density and the thickness of the element, respectively. The diagonal form of lumped mass matrix shows superiority over the consistent mass matrix in solving the dynamics equations.

6. Numerical examples

In this section, some examples will be presented to demonstrate the properties of the present method. In some cases, to emphasize the advantages of the ES-FEM, the results of the present method will be compared with those of the FEM using triangular elements (FEM-T3), 4-node quadrilateral (FEM-Q4), 8-node quadratic elements (FEM-Q8) and NS-FEM using triangular elements.

The error norm of displacement is given by Eq. (36), and the error norm of energy is calculated by

$$e_e = |E_{\text{num}} - E_{\text{exact}}|^{1/2} \tag{39}$$

where the total strain energy of numerical solution E_{num} and the total strain energy of exact solution E_{exact} is calculated by

$$E_{\text{num}} = \tfrac{1}{2}\mathbf{d}^{\text{T}}\mathbf{K}_{\text{num}}\mathbf{d} \tag{40}$$

$$E_{\text{exact}} = \frac{1}{2}\lim_{N_e\to\infty}\sum_{i=1}^{N_e}\int_{\Omega_i}\boldsymbol{\varepsilon}_i^{\text{T}}\mathbf{D}\boldsymbol{\varepsilon}_i\,\mathrm{d}\Omega \tag{41}$$

where $\boldsymbol{\varepsilon}_i$ is the strain of exact solution of the ith element. In actual computation using Eq. (41), we will use a very fine mesh ($N_e\to\infty$) to calculate the exact strain energy E_{exact}.

In the ES-FEM, the value of strains (or stresses) at the node i will be average value of strains (or stresses) of the smoothing domains $\Omega^{(k)}$ associated with edge k, and are calculated numerically by

$$\tilde{\varepsilon}_i = \frac{1}{A^{(i)}}\sum_{k=1}^{N_s^{(i)}}\tilde{\varepsilon}_k A^{(k)} \tag{42}$$

where $N_s^{(i)}$ is the total number of edges (sides) connecting directly to node i, $\tilde{\varepsilon}_k$ and $A^{(k)}$ are the strain and the area of the smoothing domain $\Omega^{(k)}$ associated with edge k around the node i, respectively, and $A^{(i)} = \sum_{k=1}^{N_s^{(i)}} A^{(k)}$.

6.1. A cantilever subjected to a parabolic traction at the free end

A cantilever with length L and height D is studied as a benchmark problem here, which is subjected to a parabolic traction at the free end as shown in Fig. 6. The cantilever is assumed to have a unit thickness so that

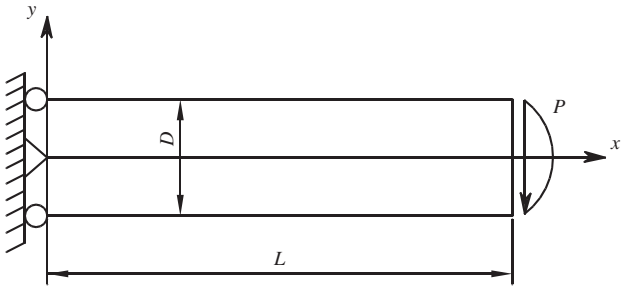

Fig. 6. A cantilever subjected to a parabolic traction at the free end.

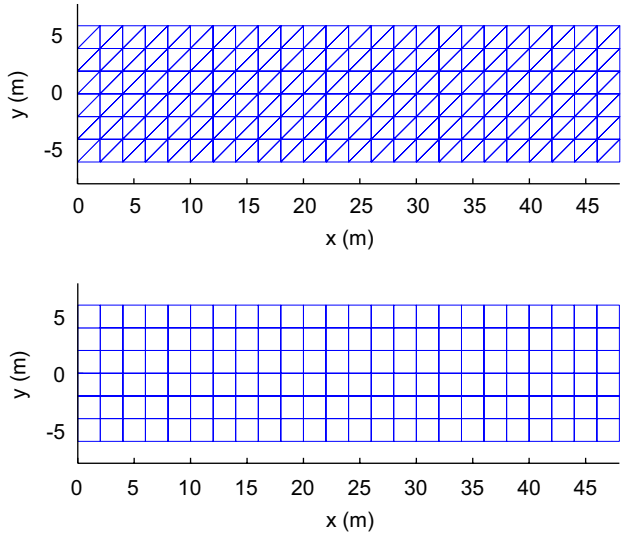

Fig. 7. Domain discretizations using triangular and 4-node quadrilateral elements of a cantilever subjected to a parabolic traction at the free end.

plane stress condition is valid. The analytical solution is available and can be found in a textbook by Timoshenko and Goodier [18].

$$u_x = \frac{Py}{6EI}\left[(6L-3x)x + (2+v)\left(y^2 - \frac{D^2}{4}\right)\right]$$
$$u_y = -\frac{P}{6EI}\left[3vy^2(L-x) + (4+5v)\frac{D^2x}{4} + (3L-x)x^2\right] \tag{43}$$

where the moment of inertia I for a beam with rectangular cross section and unit thickness is given by $I = D^3/12$.

The stresses corresponding to the displacements Eq. (43) are

$$\sigma_{xx}(x,y) = \frac{P(L-x)y}{I}, \quad \sigma_{yy}(x,y) = 0, \quad \tau_{xy}(x,y) = -\frac{P}{2I}\left(\frac{D^2}{4} - y^2\right) \tag{44}$$

The related parameters are taken as $E = 3.0 \times 10^7$ kPa, $v = 0.3$, $D = 12$ m, $L = 48$ m and $P = 1000$ N. In the computations, the nodes on the left boundary are constrained using the exact displacements obtained from Eq. (43) and the loading on the right boundary uses the distributed parabolic shear stresses in Eq. (44). Two types of meshes using triangular and quadrilateral elements are used as shown in Fig. 7.

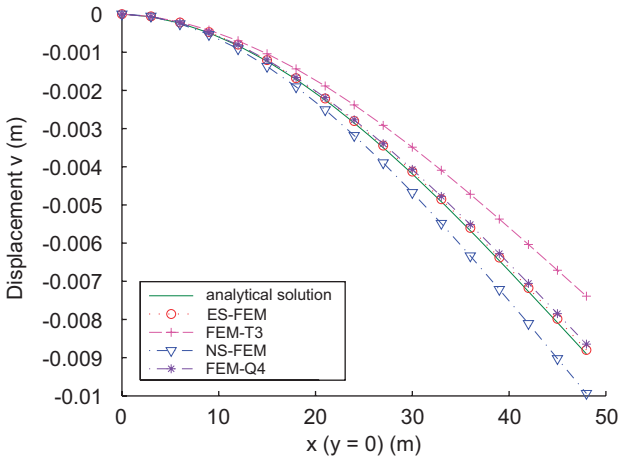

Fig. 8. Distribution of displacement v along $(x, 0)$ in a cantilever subjected to a parabolic traction at the free end.

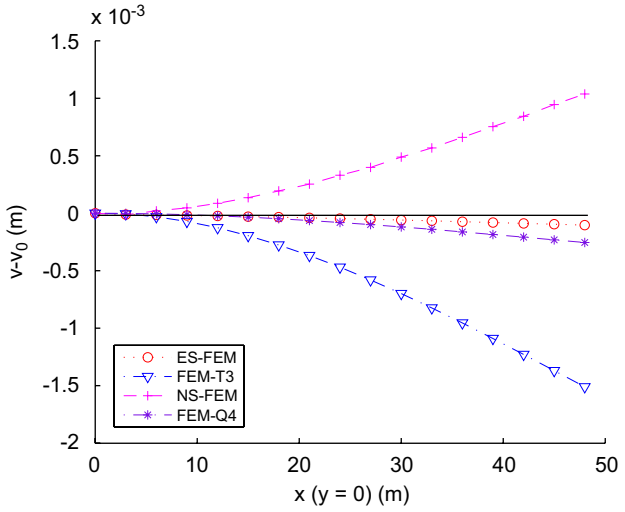

Fig. 9. Distribution of relative error in displacement v along $(x, 0)$ in a cantilever subjected to a parabolic traction at the free end.

Figs. 8 and 9 compare the results of displacements and relative errors of the ES-FEM with the FEM-T3, NS-FEM and FEM-Q4. It is shown that the FEM-T3 is very stiff while the NS-FEM is very soft compared to the exact solution. The ES-FEM is stiffer than the NS-FEM and softer than the FEM-T3, and is very close to the exact solution. Compared with all methods, the ES-FEM is best and even better than the FEM-Q4 (see Fig. 9). From Figs. 10 and 11, it is observed that all the computed stresses using the ES-FEM are in a good agreement with the analytical solutions.

The convergence of the strain energy is shown in Fig. 12, and the convergence rates of error norms in displacement and energy are demonstrated in Figs. 13 and 14. As expected, the FEM modes behave overly-stiff and hence give lower bounds, and NS-FEM behaves overly-soft and gives an upper bound. The ES-FEM has a very close-to-exact stiffness and hence the results are very accurate: the ES-FEM results are the most accurate. It is observed that all strain energy, displacement and energy error norms of the ES-FEM are even better than those of the FEM-Q4. Superconvergence is also observed for the ES-FEM: the convergence rates are much larger than the theoretical value of 2.0 in displacement norm and 1.0 in energy norm.

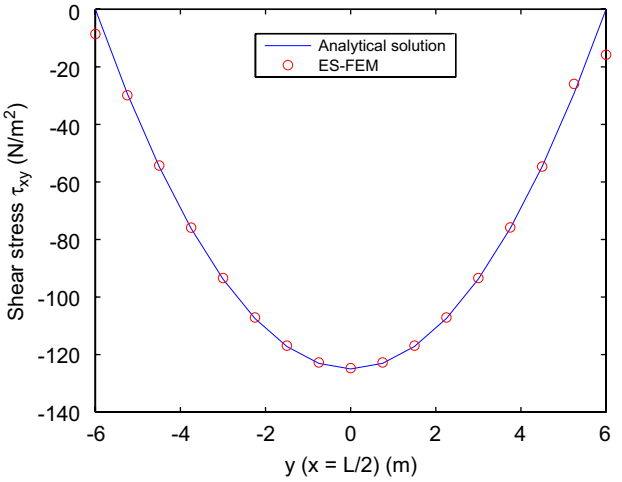

Fig. 10. Distribution of the shear stress τ_{xy} along the section of $x = L/2$ in a cantilever subjected to a parabolic traction at the free end.

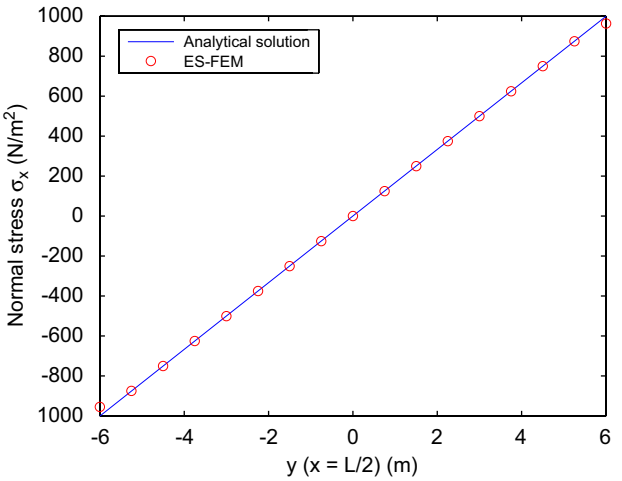

Fig. 11. Distribution of the normal stress σ_x along the section of $x = L/2$ in a cantilever subjected to a parabolic traction at the free end.

Fig. 15 compares the computation time of different methods using the same direct solver. It is found that with the same sets of nodes, the computation time of the ES-FEM is longer than those of the FEM-Q4 and the FEM-T3, but shorter than that of the NS-FEM. However, when the efficiency of computation (computation time for the same accuracy) in terms of both energy and displacement error norms is considered, the ES-FEM is the most efficient as shown in Figs. 16 and 17. These results show a special advantage of the ES-FEM against the FEM-Q4 because the ES-FEM only uses triangular elements which are very favorite and easy in automated mesh generation.

6.2. *Infinite plate with a circular hole*

Fig. 18 represents a plate with a central circular hole of radius $a = 1$ m, subjected to a unidirectional tensile load of $\sigma = 1.0$ N/m at infinity in the x-direction. Due to its symmetry, only the upper right quadrant of the plate is modeled. Plane strain condition is considered and $E = 1.0 \times 10^3$ N/m^2, $v = 0.3$. Symmetric conditions are imposed on the left and bottom edges, and the inner boundary of the hole is traction free. The analytical

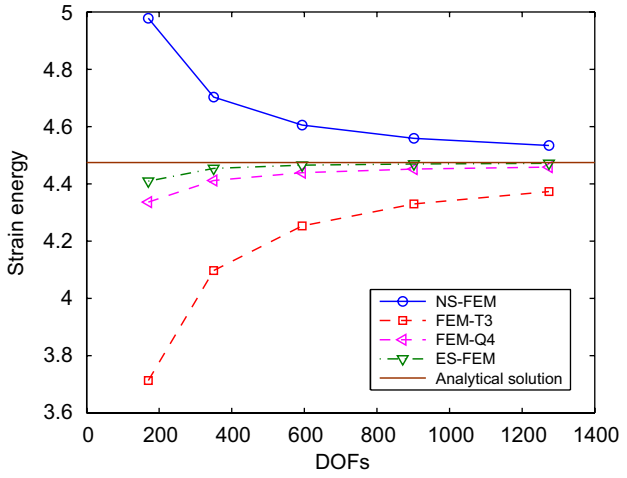

Fig. 12. Convergence of the strain energy in a cantilever subjected to a parabolic traction at the free end.

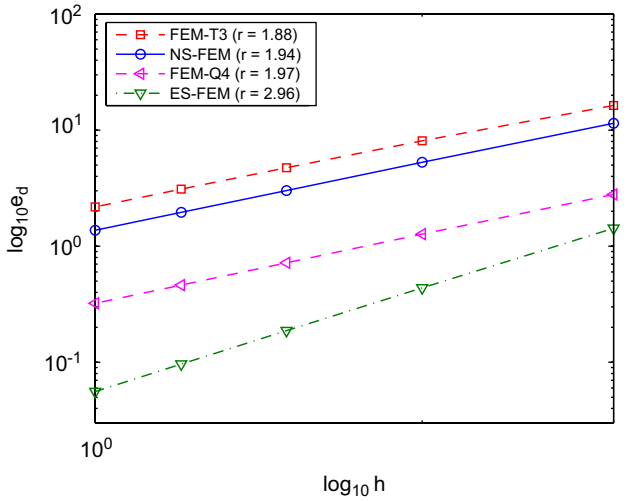

Fig. 13. Convergence rate of displacement error norms in a cantilever subjected to a parabolic traction at the free end.

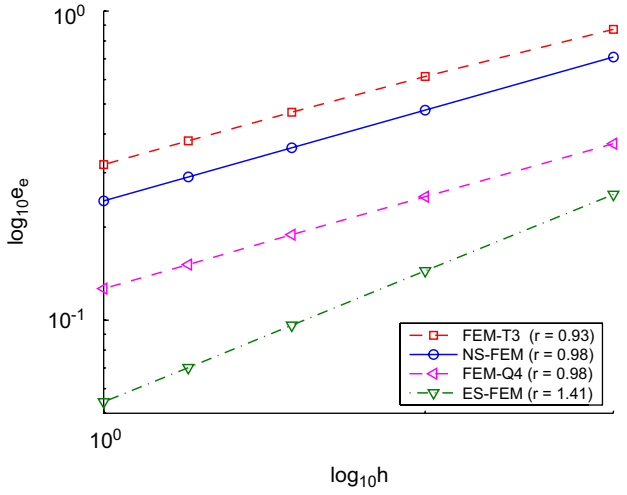

Fig. 14. Convergence rate of energy error norms in a cantilever subjected to a parabolic traction at the free end.

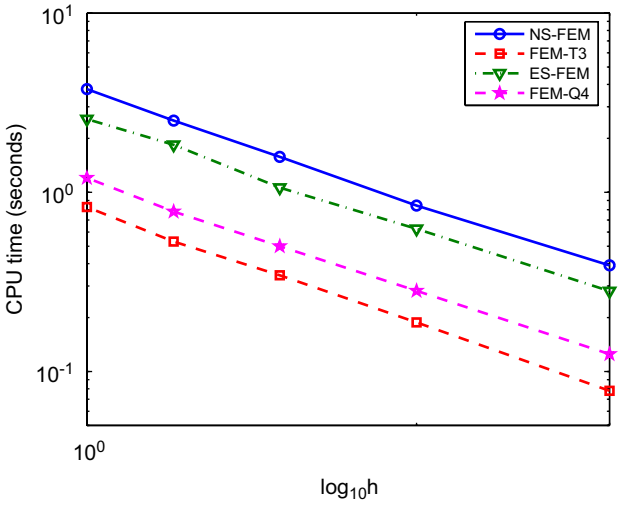

Fig. 15. Comparison of the computation time in a cantilever subjected to a parabolic traction at the free end.

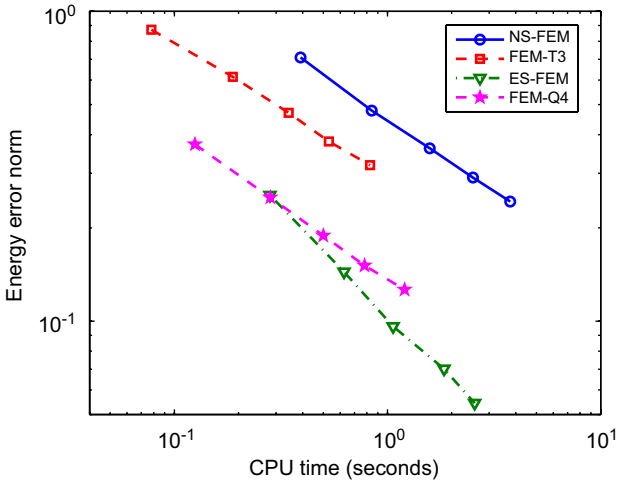

Fig. 16. Comparison of the efficiency of computation time in terms of energy error norm in a cantilever subjected to a parabolic traction at the free end.

solution for the stress is [18]

$$\sigma_{11} = 1 - \frac{a^2}{r^2}\left[\frac{3}{2}\cos 2\theta + \cos 4\theta\right] + \frac{3a^4}{2r^4}\cos 4\theta$$
$$\sigma_{22} = -\frac{a^2}{r^2}\left[\frac{1}{2}\cos 2\theta - \cos 4\theta\right] - \frac{3a^4}{2r^4}\cos 4\theta$$
$$\tau_{12} = -\frac{a^2}{r^2}\left[\frac{1}{2}\sin 2\theta + \sin 4\theta\right] + \frac{3a^4}{2r^4}\sin 4\theta \tag{45}$$

where (r, θ) are the polar coordinates and θ is measured counterclockwise from the positive x-axis. Traction boundary conditions are imposed on the right ($x = 5.0\,\mathrm{m}$) and top ($y = 5.0\,\mathrm{m}$) edges based on the exact

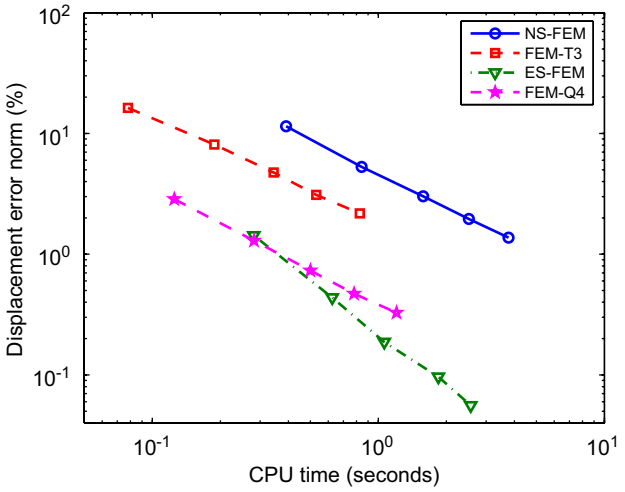

Fig. 17. Comparison of the efficiency of computation time in terms of displacement error norm in a cantilever subjected to a parabolic traction at the free end.

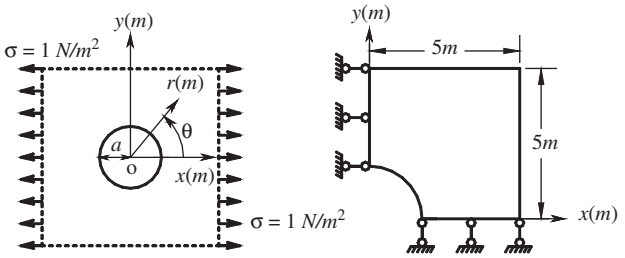

Fig. 18. Infinite plate with a circular hole subjected to unidirectional tension and its quarter model with symmetric conditions imposed on the left and bottom edges.

solution, Eq. (45). The displacement components corresponding to the stresses are

$$u_1 = \frac{a}{8\mu}\left[\frac{r}{a}(\kappa+1)\cos\theta + 2\frac{a}{r}((1+\kappa)\cos\theta + \cos 3\theta) - 2\frac{a^3}{r^3}\cos 3\theta\right]$$
$$u_2 = \frac{a}{8\mu}\left[\frac{r}{a}(\kappa-1)\sin\theta + 2\frac{a}{r}((1-\kappa)\sin\theta + \sin 3\theta) - 2\frac{a^3}{r^3}\sin 3\theta\right] \quad (46)$$

where $\mu = E/(2(1+v))$ and κ is defined in terms of Poisson's ratio by $\kappa = 3–4v$ for plane strain cases. Two types of meshes using triangular and quadrilateral elements are used as shown in Fig. 19.

Figs. 20 and 21 show the comparison of displacements of the ES-FEM with the FEM-T3, NS-FEM and FEM-Q4. It is again showed that the FEM-T3 is very stiff while the NS-FEM is very soft compared to the exact solution. The results of the ES-FEM are best and even better than those of the FEM-Q4. From Figs. 22 and 23, it is observed that all the computed stresses using the ES-FEM are in a good agreement with the analytical solutions. It is also noticed that the present stresses are very smooth though no post-processing is performed for them.

The convergence of the strain energy is shown in Fig. 24, and the convergence rates of the error norms in displacement and energy are plotted in Figs. 25 and 26. As expected, the FEM modes behave overly-stiff and hence give lower bounds, and NS-FEM behaves overly-soft and gives an upper bound. The ES-FEM has a quite close-to-exact stiffness and hence the results are very accurate: the ES-FEM results are the most accurate. It is again observed that all strain energy, and displacement and energy error norms of the ES-FEM are even better than those of the FEM-Q4. A weak superconvergence is also observed for the ES-FEM: the

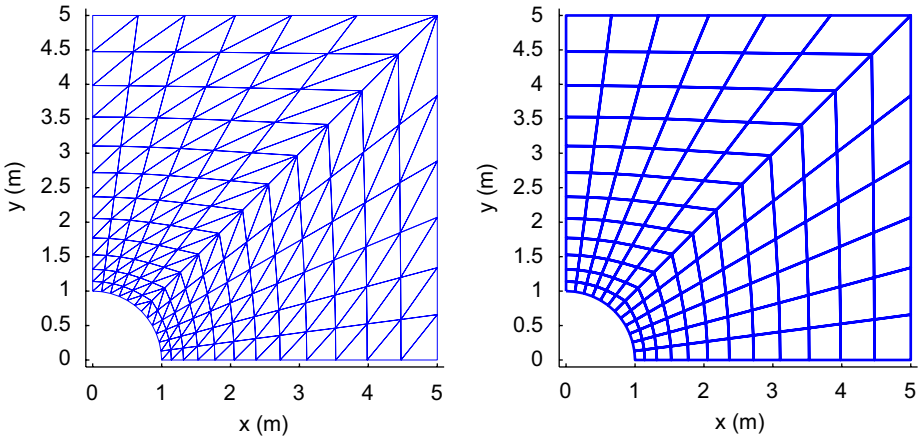

Fig. 19. Domain discretization using triangular and 4-node quadrilateral elements of the infinite plate with a circular hole subjected to unidirectional tension.

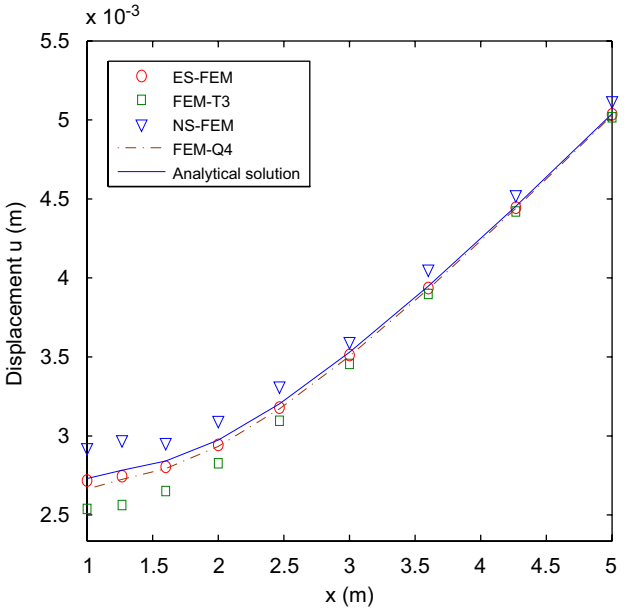

Fig. 20. Distribution of displacement u along the bottom boundary of the infinite plate with a hole subjected to unidirectional tension.

convergence rates are a little larger than the theoretical value of 2.0 in displacement norm and 1.0 in energy norm.

Fig. 27 shows the error in displacement for nearly incompressible material when Poisson's ratio is changed from 0.4 to 0.4999999. The results show that the domain-based selective ES/NS-FEM can overcome the volumetric locking for nearly incompressible materials and gives even better results than those of the NS-FEM, thanks to the super accuracy of the ES-FEM.

6.3. Free vibration analysis of a cantilever beam

In this example, a cantilever beam is studied, with $L = 100\,\text{mm}$, $H = 10\,\text{mm}$, thickness $t = 1.0\,\text{mm}$, Young's modulus $E = 2.1 \times 10^4\,\text{kgf/mm}^4$, Poisson's ratio $v = 0.3$, mass density $\rho = 8.0 \times 10^{-10}\,\text{kgf s}^2/\text{mm}^4$.

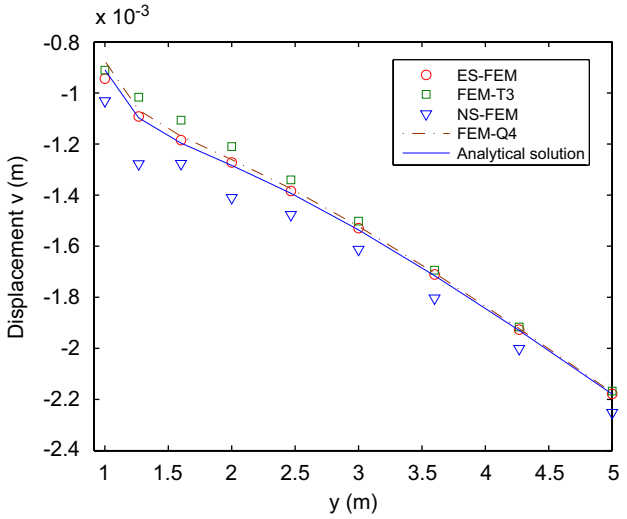

Fig. 21. Distribution of displacement v along the left boundary of the infinite plate with a hole subjected to unidirectional tension.

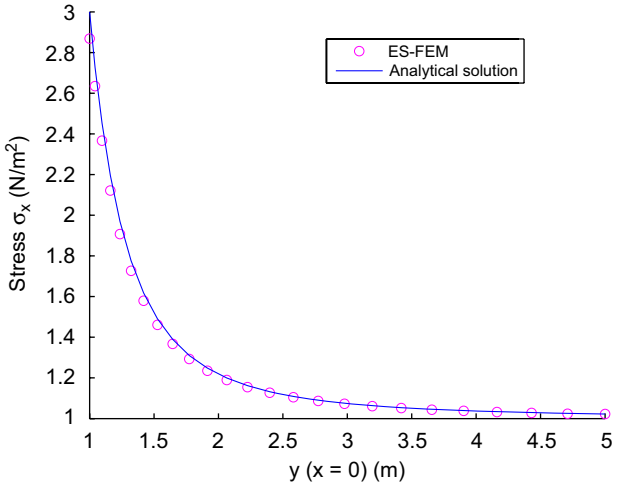

Fig. 22. Distribution of stress along the left boundary ($x = 0$) of the infinite plate with a hole subjected to unidirectional tension.

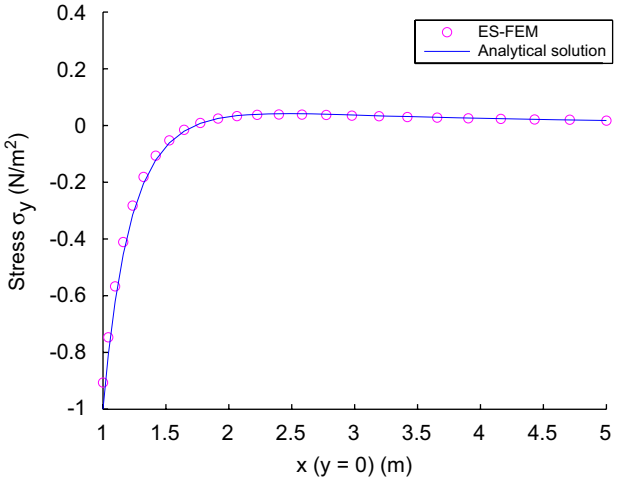

Fig. 23. Distribution of stress along the bottom boundary ($y = 0$) of the infinite plate with a hole subjected to unidirectional tension.

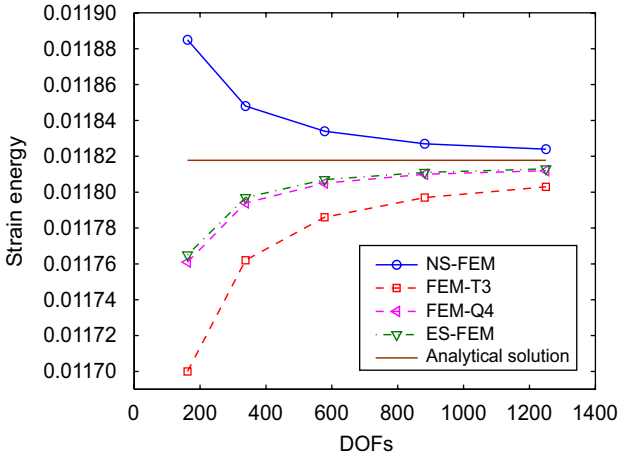

Fig. 24. Convergence of the strain energy of the infinite plate with a hole subjected to unidirectional tension.

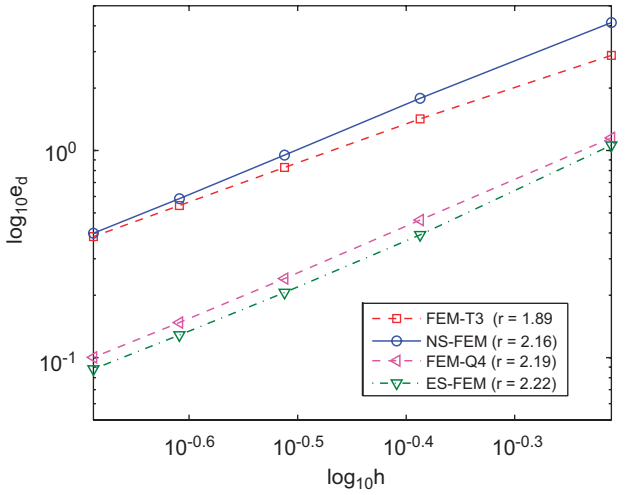

Fig. 25. Convergence rate of displacement error norms in the infinite plate with a hole subjected to unidirectional tension.

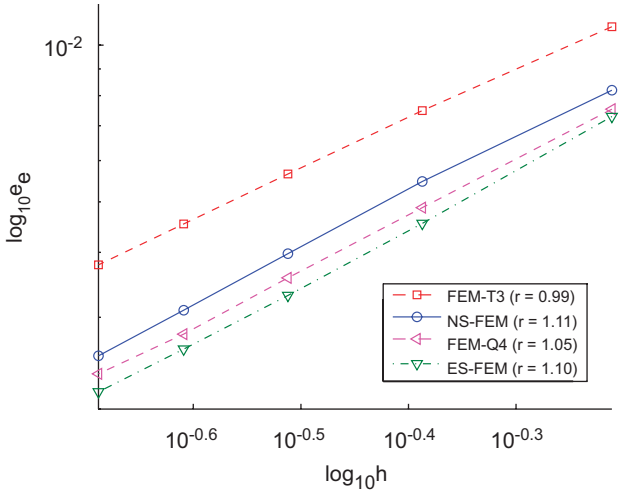

Fig. 26. Convergence rate of energy error norms in the infinite plate with a hole subjected to unidirectional tension.

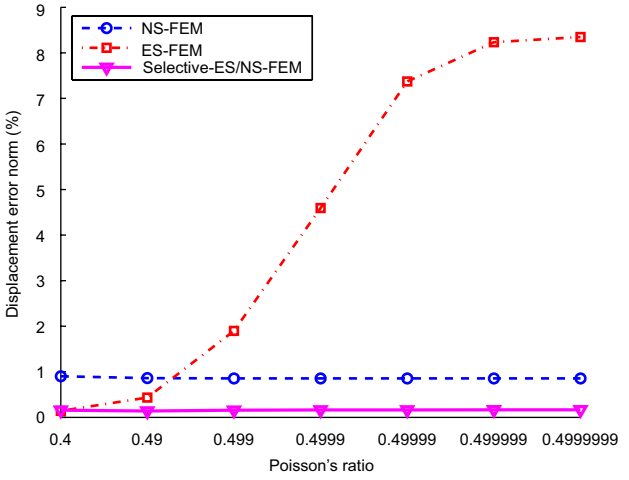

Fig. 27. Displacement error norm for materials of different Poisson's ratios in the infinite plate with a hole subjected to unidirectional tension.

Table 1
First 12 natural frequencies ($\times 10^4$ Hz) of a cantilever beam

No. of elements	No. of nodes	NS-FEM	FEM-T3	FEM-Q4	ES-FEM	Reference FEM-Q4 100×10
(10×1) 10 4-node elements for FEM-Q4 and 20 triangular elements for others methods	22	0.0576	0.1692	0.0992	0.1048	0.0824
		0.3243	0.9163	0.5791	0.6018	0.4944
		0.7441	1.2869	1.2834	1.2833	1.2824
		0.9875	2.1843	1.4830	1.5177	1.3022
		1.0112	3.5942	2.6183	2.6362	2.3663
		1.1346	3.8338	3.8140	3.7724	3.6085
		1.2783	5.0335	3.8824	3.8559	3.8442
		1.5712	6.2421	5.1924	5.0349	4.9674
		2.3697	6.4154	6.2345	6.0827	6.3960
		3.2685	7.5940	6.4846	6.1520	6.4023
		3.7064	8.4790	7.7039	7.0519	7.8853
		3.8642	8.7033	8.4632	7.7212	8.9290
(20×2) 40 4-node elements for FEM-Q4 and 80 triangular elements for others methods	63	0.0675	0.1117	0.0870	0.0853	0.0824
		0.4032	0.6539	0.5199	0.5078	0.4944
		1.0518	1.2843	1.2830	1.2828	1.2824
		1.2810	1.6748	1.3640	1.3246	1.3022
		1.6467[a]	2.9554	2.4685	2.3783	2.3663
		1.8786	3.8424	3.7477	3.5784	3.6085
		2.7823[a]	4.3866	3.8378	3.8298	3.8442
		3.0926	5.8836	5.1322	4.8533	4.9674
		3.6783	6.3751	6.3585	6.1527	6.3960
		3.8089	7.4046	6.5731	6.3182	6.4023
		4.0543[a]	8.8210	8.0342	7.4419	7.8853
		4.1605[a]	8.9411	8.8187	8.6776	8.9290
(40×4) 160 4-node elements for FEM-Q4 and 320 triangular elements for others methods	205	0.0778	0.0906	0.0835	0.0827	0.0824
		0.4654	0.5409	0.5004	0.4950	0.4944
		1.2199	1.2831	1.2827	1.2826	1.2824
		1.2818	1.4161	1.3174	1.3006	1.3022
		1.6689[a]	2.5570	2.3926	2.3554	2.3663
		2.2012	3.8433	3.6462	3.5778	3.6085
		3.2517[a]	3.8786	3.8431	3.8408	3.8442

Table 1 (*continued*)

No. of elements	No. of nodes	NS-FEM	FEM-T3	FEM-Q4	ES-FEM	Reference FEM-Q4 100×10
		3.3270	5.3087	5.0150	4.9029	4.9674
		3.8344	6.3935	6.3883	6.2867	6.3960
		4.5248	6.8093	6.4561	6.3774	6.4023
		4.6406[a]	8.3473	7.9398	7.6987	7.8853
		5.3275[a]	8.9183	8.9057	8.8751	8.9290

[a]Spurious non-zero energy modes.

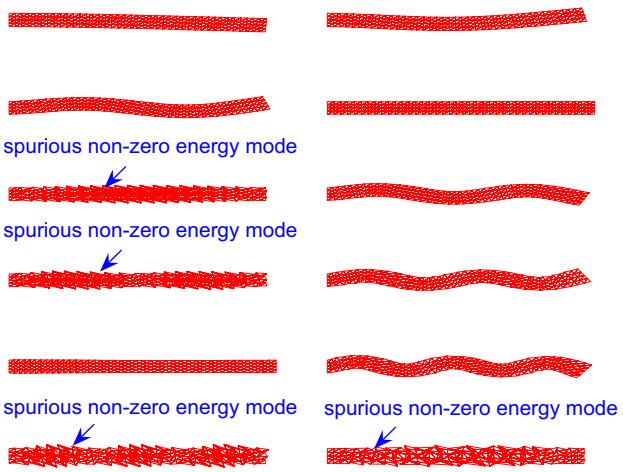

Fig. 28. First 12 modes of the cantilever beam by the NS-FEM.

A plane stress problem is considered. Using the Euler–Bernoulli beam theory we can get its fundamental frequency $f_1 = 0.08276 \times 10^4$ Hz as a reference. Three kinds of regular meshes are used in the analysis using the FEM-T3, NS-FEM, FEM-Q4 and ES-FEM for comparison purpose. Numerical results using the FEM-Q4 with a very fine mesh (100×10) for the same problem are computed and used as reference solutions.

Table 1 lists the first 12 natural frequencies of the beam, and the first 12 modes using the NS-FEM and the ES-FEM are demonstrated in Figs. 28 and 29. It is observed that (1) the ES-FEM does not have any of the spurious non-zero energy modes which appear in the NS-FEM that is known overly-soft; (2) the natural frequencies obtained using the ES-FEM is much larger than those of the FEM-T3 that is known overly-stiff and (3) the ES-FEM results are generally closest to the reference solution, and they converge faster even than the FEM-Q4 with the same sets of nodes used. Because the natural frequencies can be used as a good indicator on assessing the stiffness of a model, the above findings confirms again that the ES-FEM has very close-to-exact stiffness.

6.4. Free vibration analysis of a shear wall

In this example, a shear wall with four openings (see Fig. 30) is analyzed, which has been solved using BEM by Brebbia et al. [21]. The bottom edge is fully clamped. Plane stress case is considered with $E = 10{,}000\,\mathrm{N/m^2}$, $v = 0.2$, $t = 1.0\,\mathrm{m}$ and $\rho = 1.0\,\mathrm{N/m^3}$. Two types of meshes using triangular and quadrilateral elements are used as shown in Fig. 31. Numerical results using the FEM-Q8 with 6104 nodes and 1922 elements for the same problem are computed and used as reference solutions.

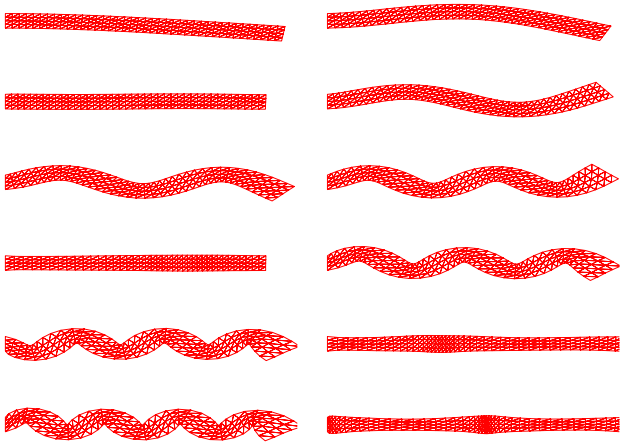

Fig. 29. First 12 modes of the cantilever beam by the ES-FEM.

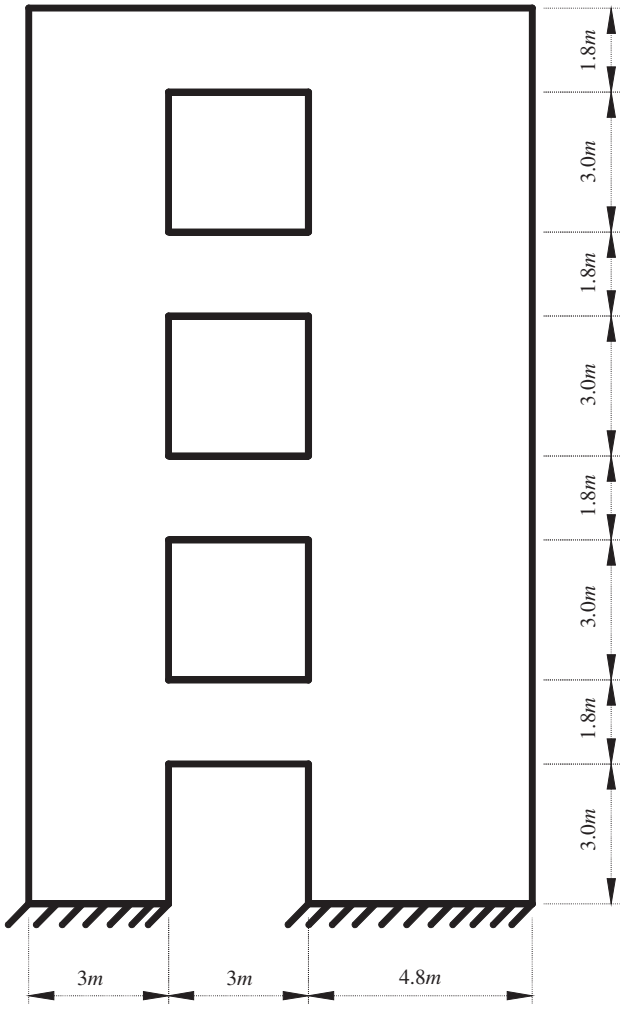

Fig. 30. A shear wall with four openings.

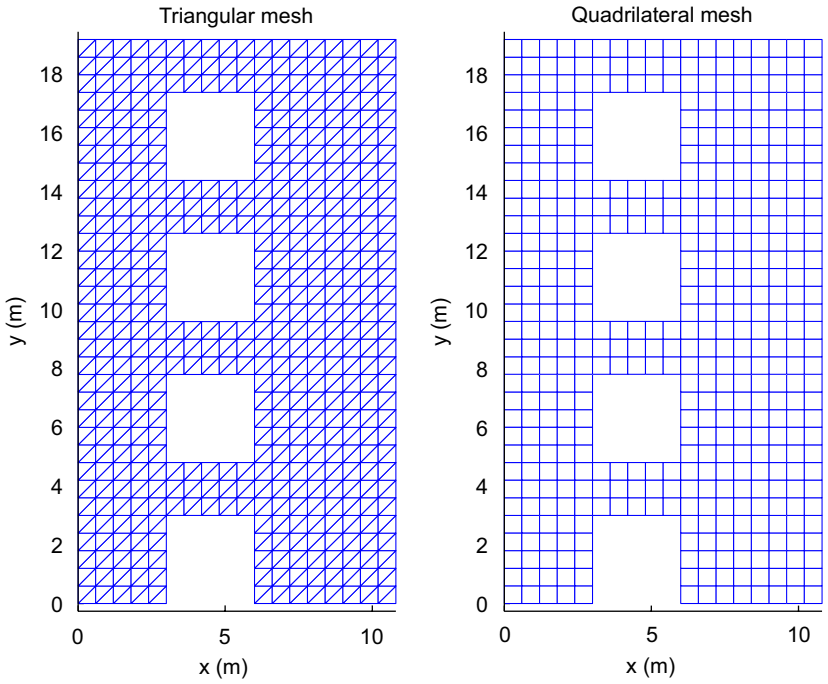

Fig. 31. Domain discretization using triangular and 4-node quadrilateral elements of the shear wall with four openings.

Table 2
First 12 natural frequencies ($\times 10^4$ Hz) of a shear wall

No. of elements	No. of nodes	NS-FEM	FEM-T3	FEM-Q4	ES-FEM	Reference (FEM-Q8) (6104 nodes 1922 elements)	Reference [21]
476 4-node elements for FEM-Q4 and 952 triangular elements for others methods	559	0.5816	0.6826	0.6599	0.6525	0.6400	0.6618
		2.0726	2.3295	2.2586	2.2402	2.2128	2.2858
		2.3920	2.4353	2.4272	2.4256	2.4192	2.4332
		3.2413	3.9959	3.7999	3.7380	3.6512	3.7666
		4.3715	5.0749	4.8831	4.8203	4.7656	5.0761
		4.6819[a]	5.9723	5.8393	5.7976	5.7506	5.9346
		5.4214	6.4878	6.3267	6.2751	6.2328	6.4515
		5.4442[a]	7.2181	7.0696	7.0009	6.9620	7.2463
		5.8441	7.5249	7.3216	7.2505	7.2052	
		6.0130[a]	7.6796	7.4967	7.4321	7.4144	
		6.1910[a]	8.1276	8.0134	7.9742	7.9634	
		6.2190[a]	8.5451	8.2987	8.2243	8.2368	
1904 4-node elements for FEM-Q4 and 3808 triangular elements for others methods	2072	0.6160	0.6567	0.6467	0.6436	0.6400	0.6618
		2.1569	2.2557	2.2278	2.2206	2.2128	2.2858
		2.4083	2.4255	2.4220	2.4211	2.4192	2.4332
		3.4679	3.7814	3.7003	3.6767	3.6512	3.7666
		4.6052	4.8771	4.8040	4.7807	4.7656	5.0761
		4.8778[a]	5.8305	5.7798	5.7640	5.7506	5.9346
		5.5872	6.3222	6.2634	6.2448	6.2328	6.4515
		5.6766[a]	7.0656	6.9986	6.9734	6.9620	7.2463
		6.0962	7.3212	7.2444	7.2196	7.0252	
		6.5288[a]	7.5023	7.4421	7.4192	7.4144	
		6.6931[a]	8.0231	7.9810	7.9672	7.9634	
		6.7808[a]	8.3447	8.2621	8.2363	8.2368	

[a]Spurious non-zero energy modes.

Table 2 lists the first 12 natural frequencies, and the first 12 modes using the NS-FEM and the ES-FEM are demonstrated in Figs. 32 and 33. It is again observed that (1) the ES-FEM does not have any of the spurious non-zero energy modes which appear in the NS-FEM that is known overly-soft; (2) the natural frequencies obtained using the ES-FEM is much larger than those of the FEM-T3 that is known overly-stiff and (3) the ES-FEM results are generally closest to the reference solution, and they converge faster even than the FEM-Q4 with the same sets of nodes used. This example confirms again that the ES-FEM has very close-to-exact stiffness.

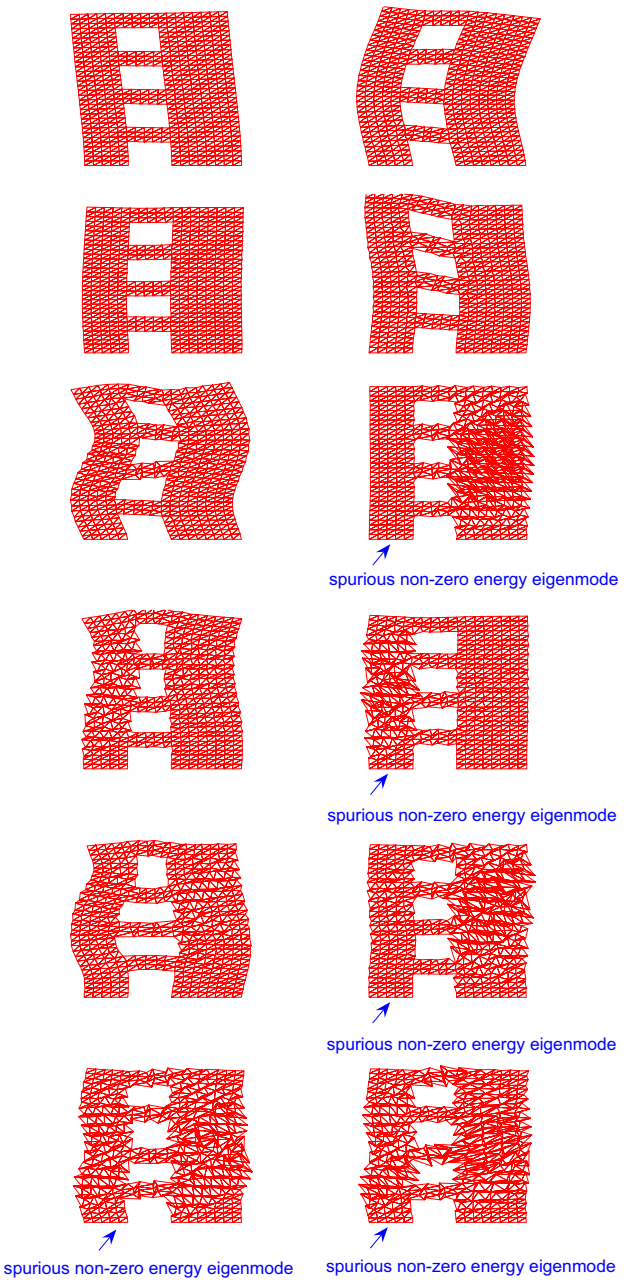

Fig. 32. First 12 modes of the shear wall by the NS-FEM.

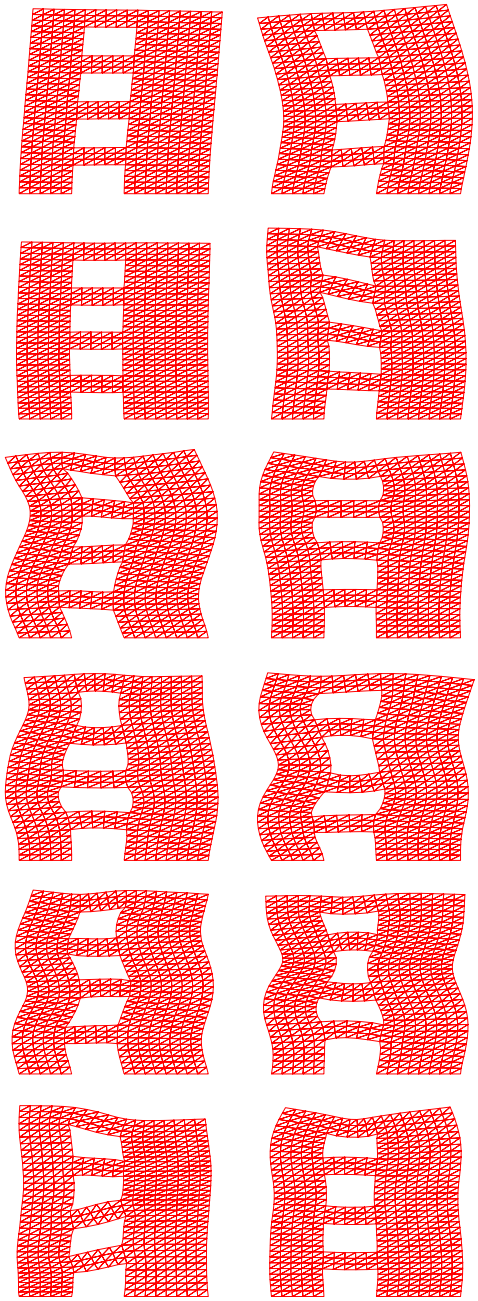

Fig. 33. First 12 modes of the shear wall by the ES-FEM.

6.5. Free vibration analysis of a connecting rod

A free vibration analysis of a connecting rod is performed as shown in Fig. 34. Plane stress problem is considered with $E = 10\,\text{GPa}$, $v = 0.3$, $\rho = 7.8 \times 10^3\,\text{kg/m}^3$. The nodes on the left inner circumference are fixed in two directions. Two types of meshes using triangular and quadrilateral elements are used as shown in Fig. 35. Numerical results using the FEM-Q4 and FEM-Q8 for the same problem are computed and used as reference solutions.

From the results in Table 3, it is observed that the ES-FEM gives the comparable results as those of the FEM-Q4 using more nodes than the ES-FEM. Again, Figs. 36 and 37 show that the ES-FEM does not have

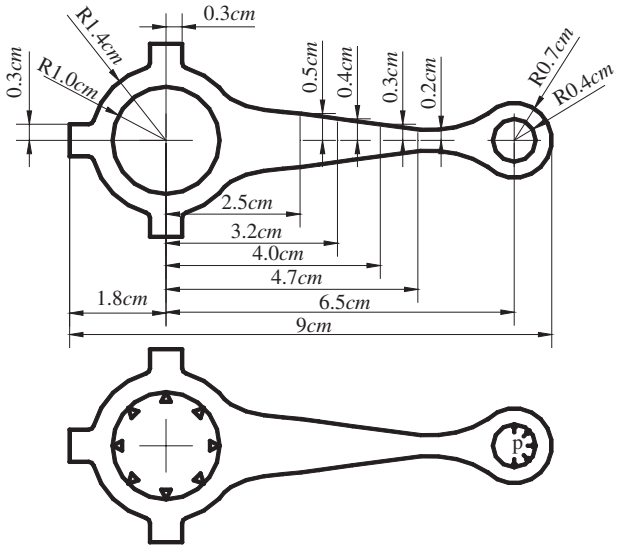

Fig. 34. Geometric model and boundary conditions of an automobile connecting bar.

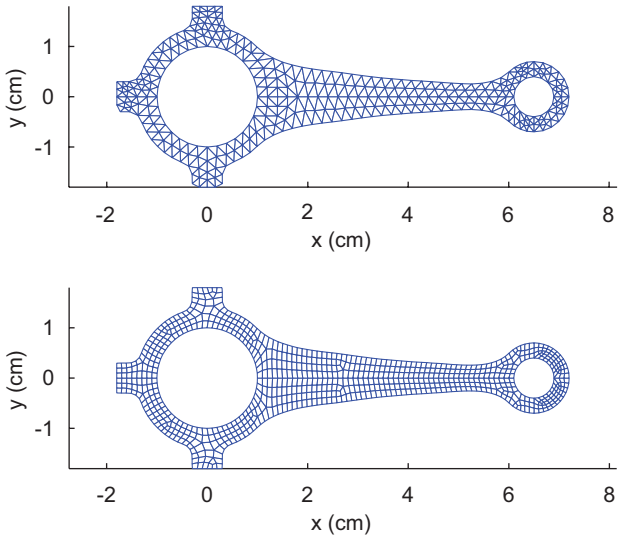

Fig. 35. Domain discretization using triangular and 4-node quadrilateral elements of the automobile connecting bar.

any of the spurious non-zero energy modes appearing in the NS-FEM. This example re-confirms the fact that ES-FEM model has very close-to-exact stiffness, and expected to perform well in vibration analysis.

6.6. *Forced vibration analysis of a cantilever beam*

A benchmark cantilever beam is investigated using the Newmark method. It is subjected to a tip harmonic loading $f(t) = \cos \omega_f t$ in y-direction. Plane strain problem is considered with non-dimensional numerical parameters as $L = 4.0$, $H = 1.0$, $t = 1.0$, $E = 1.0$, $v = 0.3$, $\rho = 1.0$, $\alpha = 0.005$, $\beta = 0.272$, $\omega_f = 0.05$, $\theta = 0.5$.[1]

[1]In Sections 6.6 and 6.7, we choose to use non-dimensional parameters because the purpose of these examples is just to examine our numerical results, and no physical implications. Any set of physical units is applicable to our results, as long as these units are consistent for all the inputs and outputs.

Table 3
First 12 natural frequencies (Hz) of a connecting bar

No. of elements	No. of nodes	NS-FEM	FEM-T3	ES-FEM	Reference (FEM-Q4) (537 nodes 429 elements)	Reference (FEM-Q4) (1455 nodes 1256 elements)	Reference (FEM-Q8) (10,002 nodes 3125 elements)
574 triangular elements (mesh 2)	373	4.9420	5.3174	5.1368	5.1369		5.1222
		20.8051	22.9448	22.0595	22.050		21.840
		48.3890	49.6982	49.3809	49.299		49.115
		48.4864	54.0642	52.0420	52.232		51.395
		84.9250	96.8632	92.7176	93.609		91.787
		97.6804	114.3134	109.5887	108.59		106.15
		114.0340	142.4456	132.6795	134.64		130.14
		123.3202[a]	163.9687	158.2376	159.45		156.14
		143.6428[a]	169.2762	158.9530	160.59		157.70
		144.6607[a]	204.5709	201.3746	203.52		200.06
		151.4276	210.1202	204.8442	208.68		204.41
		161.9533[a]	210.7405	209.2773	209.02		204.99
2296 triangular elements (mesh 3)	1321	5.0481	5.2084	5.1246		5.1244	5.1222
		21.4886	22.2661	21.8805		21.909	21.840
		48.8798	49.3544	49.1726		49.211	49.115
		50.4006	52.4947	51.5181		51.657	51.395
		89.6102	93.8422	91.9305		92.390	91.787
		92.6458[a]	109.2835	106.8473		107.51	106.15
		103.4429	134.5815	130.5546		131.48	130.14
		125.6500	159.7354	156.3497		157.51	156.14
		151.6215[a]	159.9686	157.8486		158.69	157.70
		152.0064[a]	203.3543	200.9013		201.69	200.06
		155.5444	207.5036	204.2601		206.04	204.41
		188.5849[a]	209.1795	206.5273		209.92	204.99

[a]Spurious non-zero energy modes.

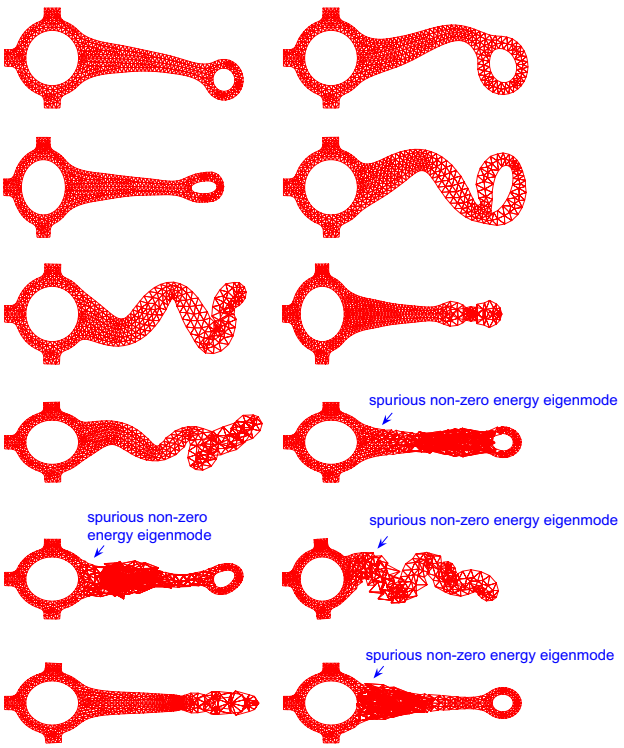

Fig. 36. First 12 modes of the connecting bar by the NS-FEM.

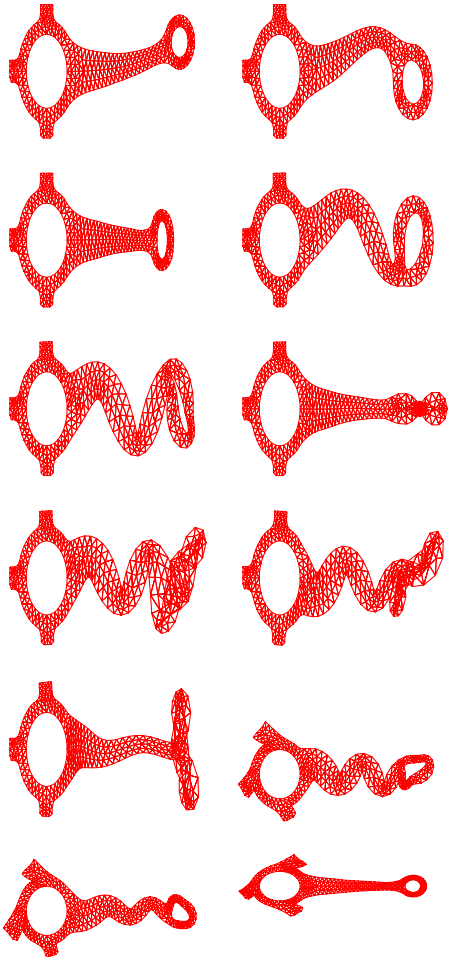

Fig. 37. First 12 modes of the connecting bar by the ES-FEM.

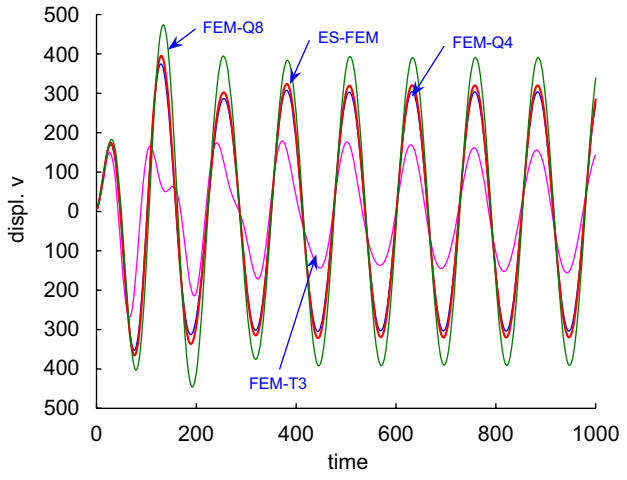

Fig. 38. Transient responses of a cantilever beam subjected to a harmonic loading.

The domain is represented with 10×4 elements. In FEM, all FEM-T3, FEM-Q4 and FEM-Q8 are used for comparison. The time step $\Delta t = 1.57$ is used for time integration. From the dynamic responses in Fig. 38, it is seen that the amplitude of the ES-FEM is closer to that of the FEM-Q8 as compared to the FEM-Q4. This shows that the ES-FEM using triangular elements can be applied to the vibration analysis with excellent accuracy. This may be partially due to the fact that ES-FEM model has very close-to-exact stiffness.

6.7. Forced vibration analysis of a spherical shell

As shown in Fig. 39, a spherical shell is studied that subjected to a concentrated loading at its apex. Two types of meshes using triangular and quadrilateral elements for half of the spherical shell are used as shown in Fig. 40. The asymmetric elements are used with non-dimensional numerical parameters given as $R = 12$, $t = 0.1$, $\phi = 10.9^\circ$, $\theta = 0.5$, $E = 1.0$, $v = 0.3$, $\rho = 1.0$. The loading is first in the harmonic form $f(t) = \cos \omega_f t$ and its dynamic responses are demonstrated in Fig. 41 with $\omega_f = 0.05$, and time step $\Delta t = 5$. No damping effect is included. Again, it is seen that the amplitude of the ES-FEM is much more accurate than that of FEM-T3, and comparable to that of the FEM-Q4. Then a constant step load $f(t) = 1$ is added at apex since $t = 0$. Without

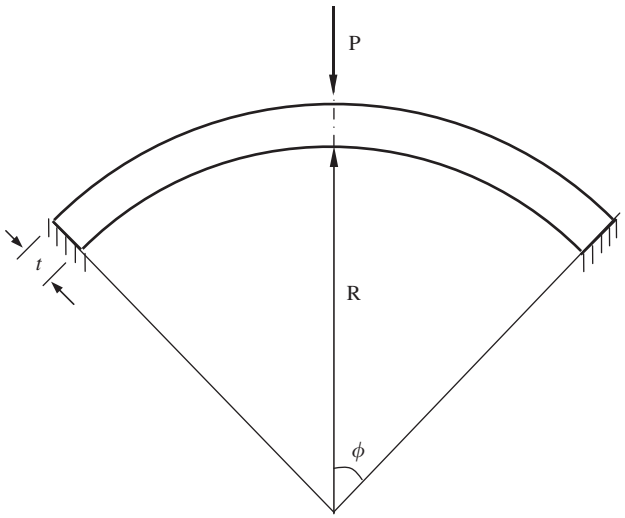

Fig. 39. A spherical shell.

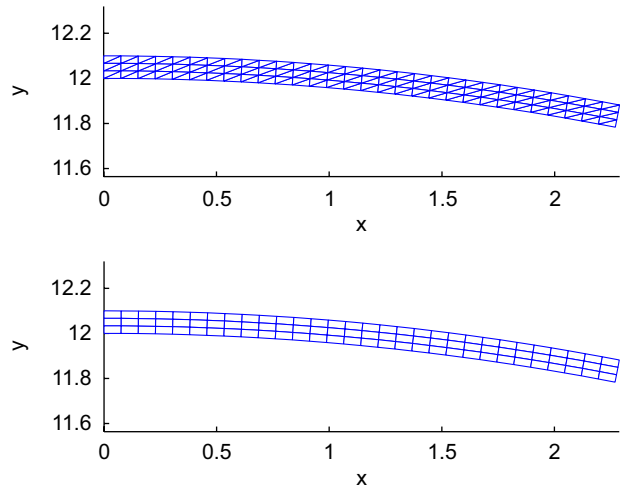

Fig. 40. Domain discretization of half of the spherical shell using triangular and 4-node quadrilateral elements.

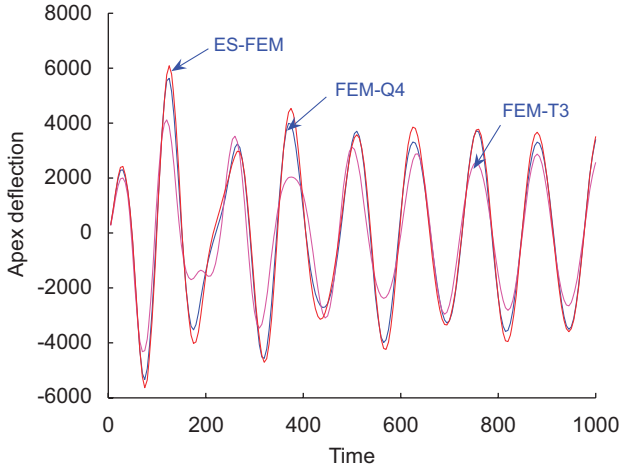

Fig. 41. Transient responses of the spherical shell subjected to a harmonic loading.

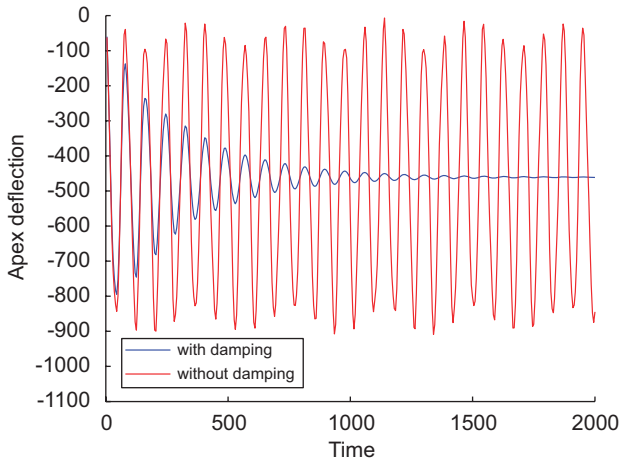

Fig. 42. Transient responses of the spherical shell subjected to a constant step loading using the ES-FEM.

damping, it is seen from Fig. 42 that the deflection at apex tends to be a constant value with the elapse of time. With the inclusion of damping ($\alpha = 0.005$, $\beta = 0.272$), the response is damped out more quickly.

7. Conclusion

In this work, an edge-based smoothed finite element method (ES-FEM) is proposed for stable and accurate solutions. The method is applied to static, free and forced vibration analyses of 2D solid mechanics problems. Through the formulation and numerical examples, some conclusions can be drawn as follows:

(a) The ES-FEM can use general n-sided polygonal elements including triangular elements. The extension of the method for 3D problems using tetrahedral elements is also straightforward.
(b) The ES-FEM using triangular elements is stable and accurate without using any parameter for stabilization. The formulation is straightforward and the implementation is as easy as the FEM, without the increase of degree of freedoms. The ES-FEM often shows superconvergence behavior with ultra-accurate results: The numerical results of the ES-FEM using triangular elements are even more accurate than the FEM using quadrilateral elements with the same sets of nodes.

(c) With the same set of nodes and the same direct solver are used, the computation time of the ES-FEM is longer than those of the FEM-Q4 and the FEM-T3, but shorter than that of the NS-FEM. However, when the efficiency of computation (computation time for the same accuracy) in terms of both energy and displacement error norms is considered, the ES-FEM is the most efficient.
(d) A domain-based selective ES/NS-FEM is effective in overcoming the volumetric locking for problems of nearly incompressible materials.
(e) For the free vibration analysis, the ES-FEM using triangular elements gives the more accurate results and higher convergence rate than the FEM-Q4. No spurious non-zero energy modes appear in vibration analysis and hence the ES-FEM is very stable temporally.
(f) For the forced vibration analysis, vibration period obtained using the ES-FEM using triangular elements is more accurate compared to the FEM-Q4, and the vibration amplitude is closer to that of the higher-order FEM-Q8.

References

[1] J.S. Chen, C.T. Wu, S. Yoon, Y. You, A stabilized conforming nodal integration for Galerkin meshfree method, *International Journal for Numerical Methods in Engineering* 50 (2000) 435–466.
[2] J.W. Yoo, B. Moran, J.S. Chen, Stabilized conforming nodal integration in the natural-element method, *International Journal for Numerical Methods in Engineering* 60 (2004) 861–890.
[3] G.R. Liu, G.Y. Zhang, K.Y. Dai, Y.Y. Wang, Z.H. Zhong, G.Y. Li, X. Han, A linearly conforming point interpolation method (LC-PIM) for 2D solid mechanics problems, *International Journal of Computational Methods* 2 (4) (2005) 645–665.
[4] G.R. Liu, Y. Li, K.Y. Dai, M.T. Luan, W. Xue, A linearly conforming radial point interpolation method for solid mechanics problems, *International Journal of Computational Methods* 3 (4) (2006) 401–428.
[5] G.R. Liu, K.Y. Dai, T.T. Nguyen, A smoothed finite element method for mechanics problems, *Computational Mechanics* 39 (2007) 859–877.
[6] G.R. Liu, T.T. Nguyen, K.Y. Dai, K.Y. Lam, Theoretical aspects of the smoothed finite element method (SFEM), *International Journal for Numerical Methods in Engineering* 71 (2007) 902–930.
[7] K.Y. Dai, G.R. Liu, T.T. Nguyen, An *n*-sided polygonal smoothed finite element method (*n*SFEM) for solid mechanics, *Finite Elements in Analysis and Design* 43 (2007) 847–860.
[8] G.R. Liu, T. Nguyen-Thoi, H. Nguyen-Xuan, K.Y. Lam, A node-based smoothed finite element method for upper bound solution to solid problems (NS-FEM), *Computers & Structures* (2008), accepted.
[9] C.R. Dohrmann, M.W. Heinstein, J. Jung, S.W. Key, W.R. Witkowski, Node-based uniform strain elements for three-node triangular and four-node tetrahedral meshes, *International Journal for Numerical Methods in Engineering* (47) (2000) 1549–1568.
[10] G.R. Liu, G.Y. Zhang, Upper bound solution to elasticity problems: a unique property of the linearly conforming point interpolation method (LC-PIM), *International Journal for Numerical Methods in Engineering* (74) (2008) 1128–1161.
[11] G.Y. Zhang, G.R. Liu, T.T. Nguyen, C.X. Song, X. Han, Z.H. Zhong, G.Y. Li, The upper bound property for solid mechanics of the linearly conforming radial point interpolation method (LC-RPIM), *International Journal of Computational Methods* 4 (3) (2007) 521–541.
[12] M.A. Puso, J. Solberg, A stabilized nodally integrated tetrahedral, *International Journal for Numerical Methods in Engineering* 67 (2006) 841–867.
[13] M.A. Puso, J.S. Chen, E. Zywicz, W. Elmer, Meshfree and finite element nodal integration methods, *International Journal for Numerical Methods in Engineering* (74) (2008) 416–446.
[14] T. Nagashima, Node-by-node meshless approach and its applications to structural analyses, *International Journal for Numerical Methods in Engineering* (46) (1999) 341–385.
[15] K.J. Bathe, *Finite Element Procedures*, MIT Press, Prentice-Hall, Cambridge, MA, Englewood Cliffs, NJ, 1996.
[16] G.R. Liu, S.S. Quek, *The Finite Element Method: A Practical Course*, Butterworth Heinemann, Oxford, 2003.
[17] O.C. Zienkiewicz, R.L. Taylor, *The Finite Element Method*, fifth ed., Butterworth Heinemann, Oxford, 2000.
[18] S.P. Timoshenko, J.N. Goodier, *Theory of Elasticity*, third ed., McGraw-Hill, New York, 1970.
[19] I.M. Smith, D.V. Griffiths, *Programming the Finite Element Method*, third ed., Wiley, New York, 1998.
[20] T.J.R. Hughes, *The Finite Element Method: Linear Static and Dynamic Finite Element Analysis*, Prentice-Hall, Englewood Cliffs, NJ, 1987.
[21] C.A. Brebbia, J.C. Telles, L.C. Wrobel, *Boundary Element Techniques*, Springer, Berlin, 1984.
[22] G.R. Liu, A generalized gradient smoothing technique and the smoothed bilinear form for Galerkin formulation of a wide class of computational methods, *International Journal of Computational Methods* 5 (2) (2008) 199–236.
[23] G.R. Liu, A weakened weak (W2) form for a unified formulation of compatible and incompatible methods, part I–Theory and part II—Application to solid mechanics problems, *International Journal for Numerical Methods in Engineering* (2008), revised.
[24] G.R. Liu, T. Nguyen-Thoi, K.Y. Lam, A novel Alpha Finite Element Method (αFEM) for exact solution to mechanics problems using triangular and tetrahedral elements, *Computer Methods in Applied Mechanics and Engineering* (197) (2008) 3883–3897.